Article

Topological temporally mode-locked laser

In the format provided by the
authors and unedited

Contents

1 Experimental Setup

We present a detailed schematic of our topological temporally mode-locked laser in Fig. 1. This figure shows the various components involved in calibrating, operating, and stabilizing the laser. In this section, we summarize these components and briefly mention their functions.

At the core of our topological temporally mode-locked laser is the "main cavity," which is the fiber laser cavity colored blue in Fig. 1. In our system, the main cavity consists of individual patch cables connected with fiber mating sleeves. All fiber in the experiment is polarization maintaining, and the patch cables are terminated with FC/APC connectors to reduce back reflections. The other optical components in the main cavity are also terminated with FC/APC connectors.

The main cavity contains two 90:10 splitters. The first splitter acts as an input to the cavity, and, when we calibrate the length of the main cavity, we couple in the pulses of an auxiliary mode-locked laser with this splitter (see Methods). This splitter recirculates 90% of the light in the cavity and couples in 10% of the light from the input port.

The second 90:10 splitter is the output port. It couples out 10% of the light from the main cavity and recirculates the remaining 90%. The light coupled out of the cavity is sent to a 50:50 splitter, and one arm of this splitter goes to a fast 5 GHz detector. The other arm goes to a second 50:50 splitter, where the power is divided between a slow (kHz) detector and a power meter. The slow detector is used to stabilize the delay lines, and the power meter enables us to monitor the power in the laser.

After the first 90:10 splitter, there is an erbium-doped fiber amplifier (EDFA), which is the source of slow laser gain in the cavity. The EDFA is followed by a 200 GHz, Channel 34 dense wavelength division multiplexing (DWDM) filter, which removes amplified spontaneous emission (ASE) when we operate the cavity below threshold and inject auxiliary pulses to calibrate the system.

After the filter, the light in the main cavity is divided at a 50:50 splitter. Half of the light continues in the main cavity (still colored blue), and the remaining light enters a common delay line path (colored brown). Another 50:50 splitter divides the light in the common delay line path between the $\pm T_{\mathrm{R}}$ delay lines. Each delay line contains three elements: an intensity modulator, which enables us to modify the pulse-to-pulse couplings produced by the delay line; a free space delay, which enables us to coarsely tune the length of the delay line; and a fiber phase shifter, which is used to stabilize the delay line. The delay lines recombine into a common path at a 50:50 splitter before finally recombining with the main cavity at another 50:50 splitter.

The remaining elements in the main cavity are a fiber stretcher, a fiber phase shifter, and an intensity modulator. The fiber stretcher and the fiber phase shifter are used to stabilize the length of the main cavity during the calibration stage, but they are unused when we operate our topological temporally mode-locked laser above threshold. We drive the intensity modulator with a ~ 250 MHz sinusoid from an RF function generator. We use a 10 MHz reference from the auxiliary laser as a clock signal for the RF function generator.

The calibration portion of our system begins at the auxiliary mode-locked laser in Fig. 1.
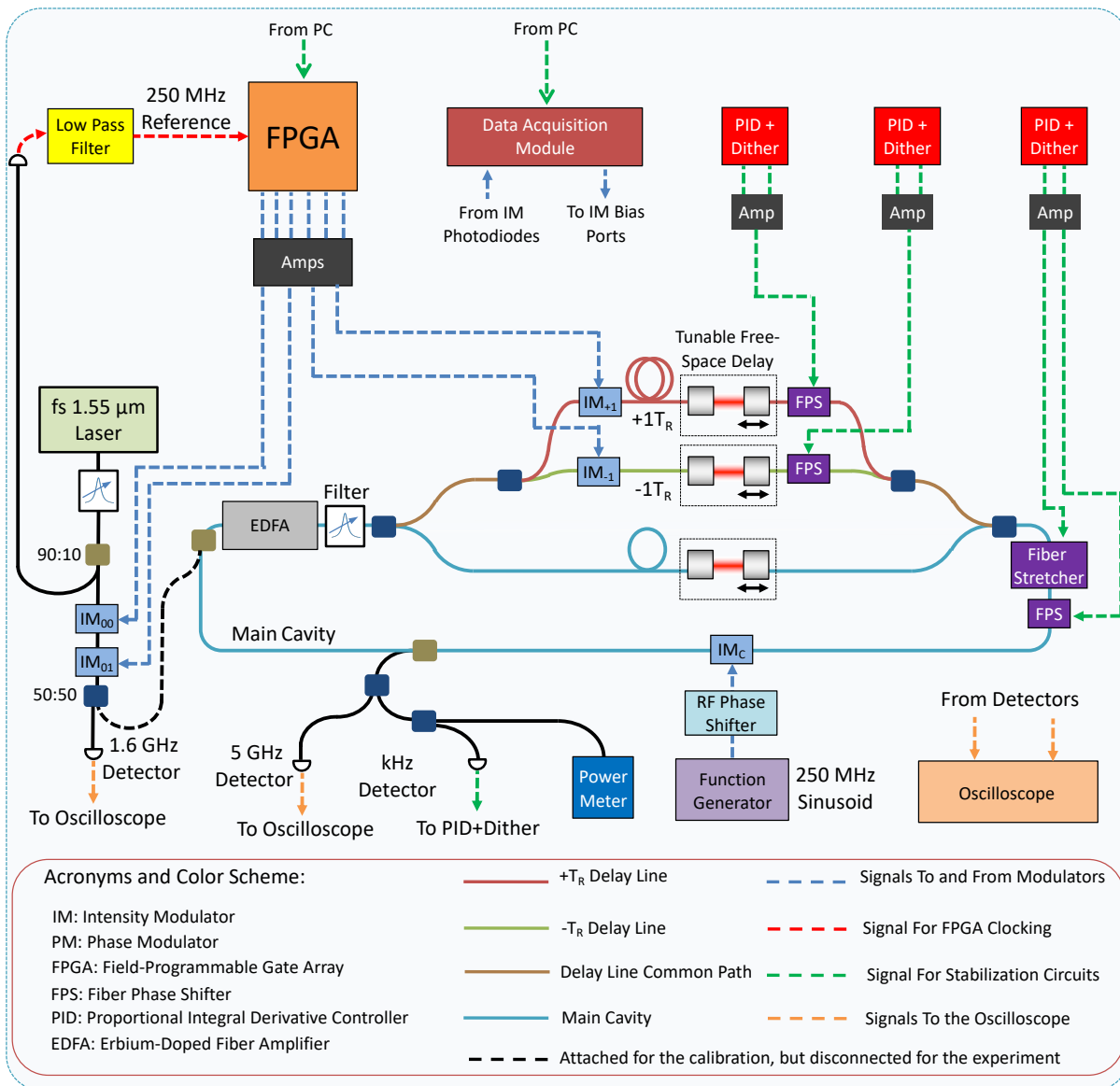
Figure 1: **Detailed Schematic of the Topological Temporally Mode-Locked Laser.**

This mode-locked laser produces femtosecond pulses at a repetition rate of ~ 250 MHz. We first send these pulses through a Channel 34 DWDM filter to stretch the pulses to ~ 5 ps. Then, we divide the stretched pulses at a 90:10 splitter.

We send the output of 10% port directly to a 600 MHz detector. The RF output of this detector passes through a 300 MHz low pass filter to generate a ~ 250 MHz clock signal for the FPGA that drives our laser's delay line intensity modulators. In this way, we lock the electronic driving signals from the FPGA to the repetition rate of our auxiliary mode-locked laser.

We send the output of the 90% port through two consecutive intensity modulators, which control the pulse pattern that we transmit into the main cavity. We use two intensity modulators to achieve a greater extinction ratio [1, 2].

After these intensity modulators, there is another 50:50 splitter in Fig. 1. This splitter is not actually present during the calibration, but it is used during our experiments. When this splitter is present, it sends 50% of the light from the auxiliary mode-locked laser to a 1.6 GHz detector, and we compare this signal to the output of our laser to determine the positions of the pulses in our synthetic lattice. We discuss the details of this positioning procedure in Sec. 3.1.

During calibration, when this 50:50 splitter is absent, the pulses from the auxiliary mode-locked laser are sent directly to the main cavity. We emphasize that this light is only injected into the main cavity during the calibration. During our experiments, we remove this external source.

To conclude this section, we summarize the electronics used to stabilize our delay lines, which are stabilized using a Pound-Drever-Hall (PDH) locking scheme [3]. The output of the slow detector in Fig. 1 is sent to several Red Pitaya STEMlabs (shown as the PID+Dither elements in Fig. 1). These devices feature built-in PDH locking capabilities, and they generate the dither and feedback signals for both delay lines. We amplify and add these signals with commercial piezo-drivers and custom PCBs, and we apply these signals to the fiber phase shifters in the delay lines. A similar procedure is used to lock the main cavity during the calibration procedure. However, there we do not sum the dither and feedback signals. Instead, we apply the dither signal to a faster fiber phase shifter, and we apply the feedback signal to the fiber stretcher, which can produce a larger phase shift.

2 Pulse Characterization

We characterize the pulses in our temporally mode-locked laser by reconstructing the pulses with a fast photodetector and by measuring the spectrum with a spectrum analyzer. For these measurements, we program the couplings of our temporally mode-locked laser to implement Hermitian nearest-neighbor couplings.

To reconstruct the pulses in the time domain, we replace the 5 GHz detector in Fig. 1 with a 30 GHz detector. This detector has a nominal impulse response of 15 ps at 1560 nm. Using this detector, we record the output of our laser on a 20 GHz oscilloscope with a 80 GSa/s sampling rate. We use the samples from the recorded trace to reconstruct the pulse envelope,
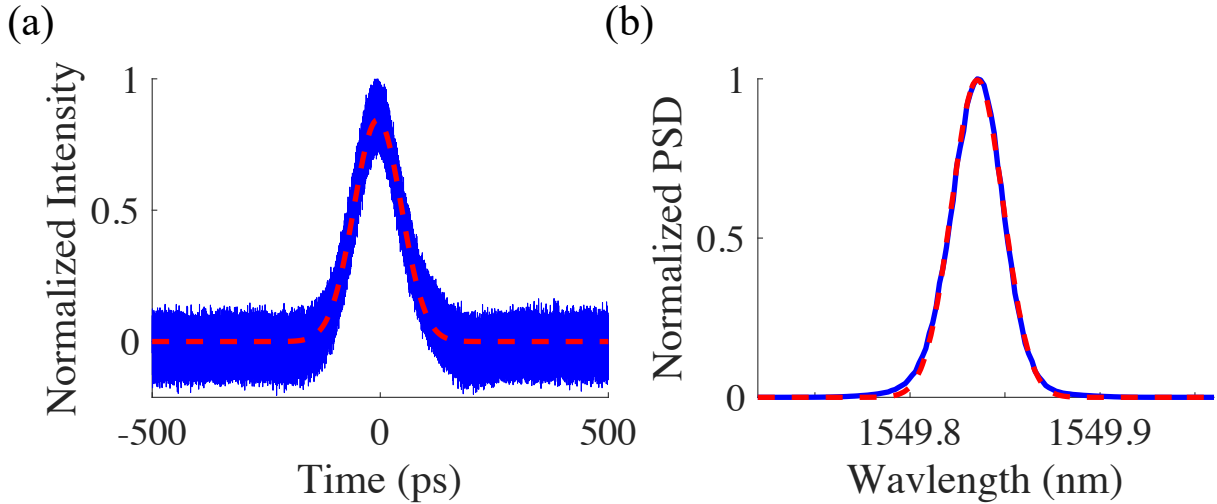
Figure 2: **Reconstruction of the Laser Pulses. (a)** Temporal reconstruction of the laser pulses in a temporally mode-locked laser with Hermitian nearest-neighbor coupling. **(b)** Power spectral density corresponding to the pulses measured in (a).

and this reconstruction is shown in Fig. 2(a). As shown by the red dashed curve, our pulse reconstruction is well fit by a Gaussian ($r^2 = 0.9675$), which reveals the width of the pulse reconstruction to be ~ 100 ps.

We show the power spectral density of the pulse train produced by our temporally mode-locked laser in Fig. 2(b). The power spectral density is also well fit by a Gaussian ($r^2 = 0.9967$).

3 Data Analysis

3.1 Positioning the Experimental Traces

An important part of analyzing the mode-locked pulse patterns in the main text is verifying that they appear where we expect them to occur in our laser's temporal synthetic lattice. This step is important because certain factors, such drift in the delay line couplings, can cause the observed pulse patterns to appear in unexpected locations. This could lead us to misidentify certain pulse patterns if the shape of the pulse pattern resembles the correct shape, but its location is incorrect.

We present an example of this situation in Fig. 3, in which we show a pulse pattern that appeared in the presence of a Hatano-Nelson domain wall in our topological temporally mode-locked laser. Theoretically, we expect that a skin mode should localize at the domain wall and, based on shape alone [Fig. 3(a)], we might conclude that observed pulse pattern does just that. However, using the positioning protocol outlined in this section, we find that the observed pulse pattern localizes to the left of the domain wall [Fig. 3(b)], likely due to an error in the applied
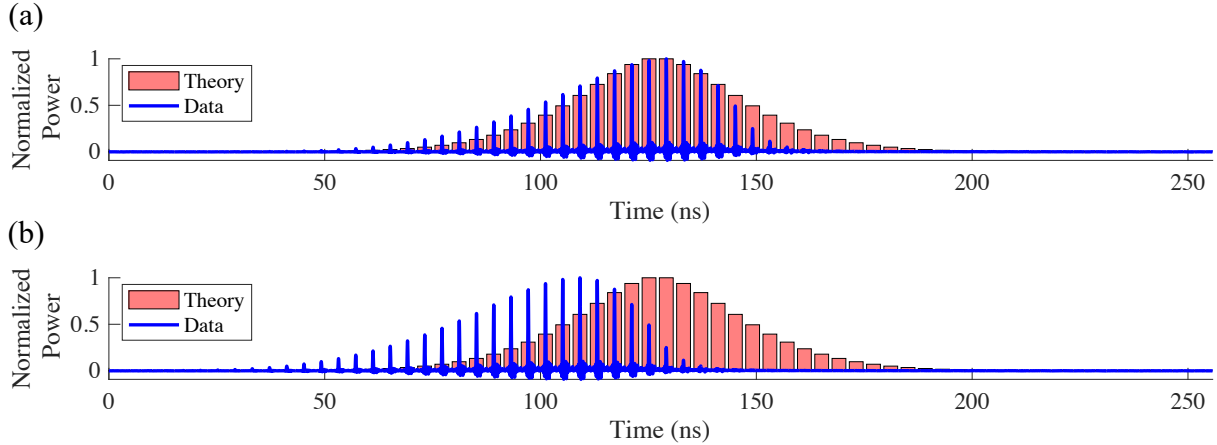
Figure 3: **Catching an Erroneously Positioned Trace.** **(a)** The observed trace is theoretically predicted to occur at a Hatano-Nelson domain wall, and, based on its shape, one might mistakenly conclude that it is indeed localized there. **(b)** The positioning protocol reveals that the trace is localized to one side of the domain wall. The disagreement between the observed trace and the theory likely arises due to an error in the applied couplings.

couplings.

Our positioning procedure relies on the auxiliary mode-locked laser introduced in Sec. 1. During an experiment, we program one of the intensity modulators outside of the main cavity in to transmit one of every 64 pulses to the 1.6 GHz detector shown in Fig. 1. Because our topological temporally mode-locked laser supports 64 pulses and has the same repetition rate as the auxiliary mode-locked laser, the reference pulses detected on the 1.6 GHz detector provide a reference from which we can determine the positions of the pulses in the lattice [see Fig. 4].

To use these reference pulses, we determine the position of the reference pulses relative to the 32nd timeslot defined by the coupling waveform, which is the pulse directly to the left of the domain wall in Fig. 3. We do this by configuring the 50:50 splitter outside of the cavity in Fig. 1 to transmit light both through the main cavity and to the 1.6 GHz detector. We launch a pulse through the splitter in what was defined to be the 32nd timeslot in our calibration, and we observe both the signal directly from the 50:50 splitter and the signal that traveled through the cavity on our oscilloscope. We measure the difference between the arrival times of the pulses from each path and account for the delay through the 50:50 splitter[1] to estimate the delay between the reference pulses and the 32nd timeslot of the main cavity. With this procedure, we estimate the delay between the reference pulses and the 32nd timeslot to be ~ 104.7 ns.

In our experiments, we observe some discrepancies between this estimated delay and the delay we measure between the reference pulses and the mode-locked pulses generated in the

---

[1]As we mentioned in the Sec. 1, this 50:50 splitter is not present during our calibration (when we define the 32nd time slot in the main cavity), but it is present during the experiment.
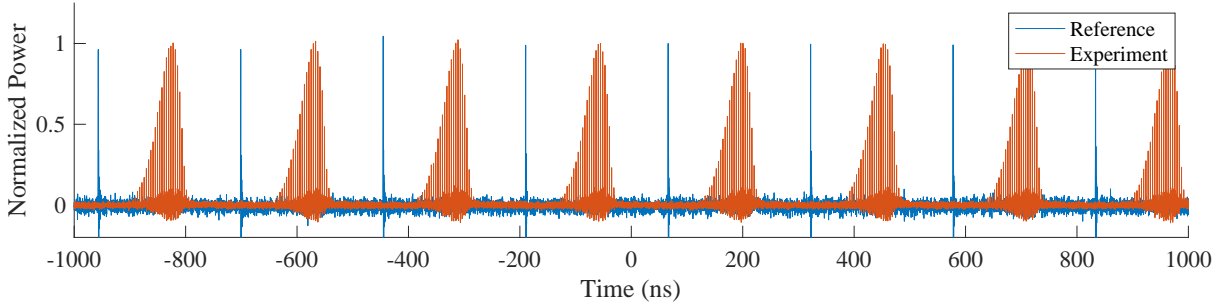
Figure 4: **Reference Signal for Positioning Traces.** We determine the position of the mode measured in Fig. 3 using a reference pulse from our auxiliary mode-locked laser, which has the same repetition rate as our topological temporally mode-locked laser. On each roundtrip of our topological temporally mode-locked laser, we view one pulse from the auxiliary mode-locked laser on our oscilloscope, and this pulse acts as a reference to determine the positions of the pulses in our synthetic temporal lattice.

32nd timeslot of our synthetic lattice. We believe that these discrepancies arise because, during our calibration procedure, we tune the phase of the RF drive applied to the intensity modulator in the main cavity (see Methods). Changing the phase of this drive changes the positions of the mode-locked pulses in the main cavity.

Due to these discrepancies, we use the following procedure to compare our measured traces with the theoretically predicted states: First, we use the estimated position of the 32nd timeslot to ballpark the position of the 32nd pulse in our synthetic lattice. Then, we use the shape of the observed pulse pattern to resolve any residual ambiguity about where the 32nd pulse occurs. Using this procedure, we measure the delay between the reference pulse and the 32nd pulse in the Hatano-Nelson nascent skin mode to be ~ 105.2 ns, and we measure the delay between the reference pulse and the 32nd pulse in the NH-SSH skin mode to be ~ 107.2 ns.

While the measured delay in the case of the NH-SSH skin mode differs from the estimated delay by ~ 2.5 ns, we recall that the pulse repetition period in our mode-locked laser is 4 ns. Therefore, depending on where the RF driving signals overlap with the optical pulses in the delay line intensity modulators, there can be up to a roughly 4 ns window in which the 32nd pulse sees the correct couplings. Given the excellent agreement between the observed data and the theoretically predicted state, we have strong reason to believe that the pulse we identified as the 32nd pulse sees the correct couplings for the 32nd time window.

3.2 Plotting the Experimental Traces

Here, we summarize the procedures used to generate the averaged heat maps and data traces presented in the main text.

To produce the heat maps shown in Main Text Fig. 2, Main Text Fig. 4, and Extended Data

7

Fig. 1, we first apply the positioning procedure described above. Then we compute the maximum value in each timeslot. We divide the maxima into different roundtrips and normalize the power in each roundtrip by dividing each maximum by the largest maximum on that roundtrip. Next we subtract an offset value to account for the presence of noise in our data. Following this we assign each maximum to be the amplitude of a Gaussian pulse whose width is chosen to be easily visible on the final heat map. We arrange the Gaussian pulses that correspond to the pulse maxima on a single roundtrip into a single row of the heat map, and we construct the full heat map by assembling the rows for all the roundtrips under study.

The averaged data traces in Main Text Fig. 2 and Main Text Fig. 3 illustrate the correspondence between the observed pulse patterns and the theoretically predicted states. To generate these plots, we divide the data trace under study into roundtrips, and we normalize the data from each roundtrip. Normalizing the traces in this manner removes any fluctuations in the power and enables us to more directly compare the pulse patterns observed on different roundtrips. Next, we average over the normalized roundtrip traces. Finally, we normalize the averaged trace so that we can compare our result with the theoretically predicted pulse pattern.

For the NH-SSH skin mode plotted in Main Text Fig. 2, the theoretical state is the lowest-loss right eigenstate corresponding to the domain wall described in the main text. On the other hand, the theoretical state for Main Text Fig. 3(d) is generated using a fitting procedure because it is difficult to accurately calibrate the boundary conditions of our Hatano-Nelson lattice. To perform this fitting procedure, we first assume that we correctly implement the desired coupling ratio $w/v = \sqrt{2}$ for the Hatano-Nelson model under consideration. We then compute the lowest-loss right eigenstate of the Hatano-Nelson lattice as we sweep the coupling between the first and final sites of the Hatano-Nelson lattice from open boundary conditions to periodic boundary conditions. At each point in the sweep, we compute the 2-norm of the difference between the theoretical lowest-loss state and the measured pulse amplitudes, and we consider the state that corresponds to the smallest 2-norm to be our best fit state. With this procedure, we find that the best fit occurs when the coupling between the first and final lattice sites is suppressed by a factor of ~ 11.6, which is reasonable given that our delay line intensity modulators have a nominal DC power extinction ratio of 22 dB.

4   Master Equation Description of Temporal Mode-Locking

4.1   Derivation of the Tight-Binding Model

In this section, we derive the tight-binding model presented in the main text. As our starting point, we propose a modified master equation for active mode-locking. This master equation has the form,

$$\frac{\partial \psi(T,t)}{\partial T} = \left(g - \ell + D_{\mathrm{g}}\frac{\partial^2}{\partial t^2} - \Delta_{\mathrm{IM}}\left(1 - \cos(\omega_{\mathrm{rep}}t)\right) \right)\psi(T,t)$$

$$+ \sum_{r}^{N} \kappa_r(t)\psi(T, t - rT_{\mathrm{RT}}/N) \quad \text{(1a)}$$

$$\frac{\partial g}{\partial T} = -\gamma\left(g - g_0 + \frac{g}{T_{\mathrm{RT}}}\int_{-T_{\mathrm{RT}}/2}^{T_{\mathrm{RT}}/2} |\psi(T,t)|^2 dt \right). \quad \text{(1b)}$$

Here $\psi(T,t)$ represents the field in the laser, g represents the laser gain, ℓ represents the roundtrip loss, D_{g} describes the gain bandwidth, Δ_{IM} describes the modulation depth, T_{RT} is the cavity roundtrip period, $\omega_{\mathrm{rep}} = 2\pi N/T_{\mathrm{RT}}$ is the angular frequency corresponding to the repetition rate of the laser, g_0 is the small signal gain, and $\gamma = T_{\mathrm{RT}}/T_{\mathrm{rel}}$ is the ratio of the roundtrip period to the gain relaxation time. The fast time t describes the time within a single roundtrip and the slow time T describes the evolution of the field from roundtrip to roundtrip. The functions $\kappa_r(t)$ describe the intracavity couplings between the different pulses in the laser. While, in our experiments, we only consider nearest-neighbor couplings, in our master equation we allow for all-to-all couplings between the pulses.

There are two primary differences between this modified master equation and the traditional master equation used to model actively mode-locked lasers [4]. First, while the traditional master equation is used to model a single mode-locked pulse, here our master equation models multiple pulses. Second, we introduce our intracavity coupling term into the master equation. This term is responsible for producing temporal mode-locking in the laser.

In practice, our experiment operates beyond several of the assumptions that go into deriving the master equation, such as the roundtrip gain and the roundtrip loss being small [4]. Nonetheless, we find that this modified master equation provides a convenient model to qualitatively analyze the behavior of our temporally mode-locked laser. Indeed, as we saw in the main text, the predictions of our modified master equation can agree quite well with what we observe in experiment. To verify that the predictions of the master equation hold beyond the assumptions that go into its derivation, we also perform lumped element simulations in Sec. 5.

To derive the tight-binding model presented in the main text from our modified master equation, we begin by assuming that the N pulses described by the equation are localized in their respective "gain wells," by which we mean that the pulses are localized near the minimum loss introduced by the cosine term in Eq. 1a. In this case, we can break Eq. 1a into N separate equations of the form,

$$\frac{\partial \psi_n(T,t)}{\partial T} = \left(g - \ell + D_{\mathrm{g}}\frac{\partial^2}{\partial t^2} - \frac{\Delta_{\mathrm{IM}}}{2}\left(\omega_{\mathrm{rep}}^2 t^2\right) \right)\psi_n(T,t) + \sum_{m=1}^{N} \kappa_{nm}\psi_m(T,t). \quad \text{(2)}$$

Here we implicitly redefine the fast time t to center each pulse at $t = 0$ in its own time window. The subscripts m and n label the fields of the different pulses.

The solutions to Eq 2 are Hermite-Gaussians, which allows us to expand $\psi_n(T, t)$ as

$$\psi_n(T, t) = \sum_k C_{nk}(T) H_k(\eta t) e^{-\eta^2 t^2 / 2}, \tag{3}$$

where $H_k(\eta t)$ is the kth-order Hermite polynomial, and the coefficients $C_{nk}(T)$ and η have yet to be determined.

Plugging Eq. 3 into Eq. 2, we find that $\eta^2 = \omega_{\text{rep}} \sqrt{\Delta_{\text{IM}}/2D_{\text{g}}}$ and

$$\frac{\partial C_{nk}}{\partial T} = \left[(g - \ell) - \omega_{\text{rep}} \sqrt{\frac{D_{\text{g}} \Delta_{\text{IM}}}{2}} (2k + 1) \right] C_{nk} + \sum_m \kappa_{nm} C_{mk}. \tag{4}$$

In the steady state, $\partial C_{nk}(T)/\partial T = 0$, and we observe that only the $k = 0$ term is nonzero. The reason for this is that, if $\partial C_{n0}(T)/\partial T = 0$, the coefficients $C_{nk}(T)$ with $k > 0$ experience net loss. On the other hand, if $\partial C_{nk}(T)/\partial T = 0$ for $k > 0$, then $C_{n0}(T)$ experiences net gain and will experience net gain until $\partial C_{n0}(T)/\partial T = 0$. Therefore, to study the steady-state behavior of the pulses, we only need to consider the Gaussian solutions to Eq. 2. With this in mind, we will now drop the subscript k and let $C_{n0} \rightarrow C_n$.

We can also rewrite our expression for the gain (Eq. 1b) in terms of the amplitudes C_n. We rewrite Eq. 1b as

$$\frac{\partial g}{\partial T} = -\gamma \left(g - g_0 + \frac{g}{T_{\text{RT}}} \int_{-\infty}^{\infty} \sum_n |\psi_n(T, t)|^2 \, dt \right). \tag{5}$$

Here we have used the assumption that the pulses are strongly localized in their respective gain wells to take the limits on the integral to infinity. We plug in our Gaussian solution from above and find that

$$\frac{\partial g}{\partial T} = -\gamma \left(g - g_0 + \frac{g}{T_{\text{RT}}} \int_{-\infty}^{\infty} \sum_n |C_n(T)|^2 \, e^{-\eta^2 t^2} dt \right). \tag{6}$$

Defining $\epsilon = \sqrt{\pi}/(\eta T_{\text{RT}})$, we arrive at the expression

$$\frac{\partial g}{\partial T} = -\gamma \left(g - g_0 + g\epsilon \sum_n |C_n(T)|^2 \right). \tag{7}$$

Combining Eq. 7 with our equation of motion for $C_n(T)$, we arrive at the desired nonlinear tight-binding model, which can be reduced to that presented in the main text:

$$\frac{\partial \mathbf{C}}{\partial T} = \left[g - \ell - \omega_{\text{rep}} \sqrt{\frac{D_{\text{g}} \Delta_{\text{IM}}}{2}} \right] \mathbf{C} + K\mathbf{C} \tag{8a}$$

10

$$\frac{\partial g}{\partial T} = -\gamma \left(g - g_0 + g\epsilon \sum_n |C_n(T)|^2 \right). \tag{8b}$$

Here $\mathbf{C}$ is a vector of the pulse amplitudes C_n, and K is a matrix with the entries $K_{nm} = \kappa_{nm}$.

4.2 Steady-State Behavior of the Tight-Binding Model

To understand the behavior of our modified master equation, we now derive the steady-state behavior of the tight-binding model in Eq. 8. We begin by assuming that the eigenvalues of K are nondegenerate. In this case, we diagonalize Eq. 8a in the right eigenbasis of K. In particular, we define a biorthogonal basis consisting of the right and left eigenvectors of K, and we define the matrices Ψ and Φ such that the columns of Ψ are the right eigenvectors of K and the rows of Φ are the left eigenvectors of K. Then, noting that $\Psi\Phi = \Phi\Psi = I$, where I is the identity, we write

$$\frac{\partial \mathbf{a}}{\partial T} = [\Lambda + g - \chi]\,\mathbf{a} \tag{9a}$$

$$\frac{\partial g}{\partial T} = -\gamma \left(g - g_0 + g\epsilon \sum_n \left| \sum_m \Psi_{nm} a_m \right|^2 \right), \tag{9b}$$

where $\chi = \ell + \omega_{\text{rep}}\sqrt{D_{\text{g}}\Delta_{\text{IM}}/2}$, $\mathbf{a} = \Phi\mathbf{C}$, and $\Lambda = \Phi K\Psi$ is the diagonal matrix whose entries are the eigenvalues of K.

Next, we rewrite Eq. 9 in terms of real-valued equations for the amplitudes and phases of the fields a_j. Letting $a_j = A_j e^{i\xi_j}$ and $\Lambda_{jj} = \lambda_j e^{i\Gamma_j}$, we find that

$$\frac{\partial A_j}{\partial T} = [\lambda_j \cos(\Gamma_j) + g - \chi]\,A_j \tag{10a}$$

$$\frac{\partial g}{\partial T} = -\gamma \left(g - g_0 + g\epsilon \sum_n \left| \sum_m \Psi_{mn} a_m \right|^2 \right) \tag{10b}$$

$$\frac{\partial \xi_j}{\partial T} = \lambda_j \sin(\Gamma_j). \tag{10c}$$

To determine the steady-state behavior of the temporally mode-locked laser, we find the fixed points of Eq. 10. We find that the steady-state pulse pattern occurs when

$$\lambda_j \cos(\Gamma_j) - \chi + \frac{g_0}{1 + \epsilon \sum_n |\sum_m \Psi_{nm} a_m|^2} = 0. \tag{11}$$

11

In practice, this condition can always be satisfied because, in our laser, χ is at least as small as the largest magnitude of any of the eigenvalues λ_j. This occurs because the coupling losses associated with the system's dissipative couplings contribute to the magnitude of χ and enforce that $\chi > \lambda_j \cos(\Gamma_j)$ for all j. Therefore, we can achieve equality in Eq. 11 by suitably choosing the value of $\sum_n |\sum_m \Psi_{nm} a_m|^2$.

To determine the steady-state value of the quantity $\sum_n |\sum_m \Psi_{nm} a_m|^2$, we first observe that Eq. 11 can only be satisfied by a single nonzero A_j as long as $\lambda_m \cos(\Gamma_m) \neq \lambda_k \cos(\Gamma_k)$ for any A_m and A_k. Assuming that this is true, we observe from Eq. 10a that the only amplitude A_j that can correspond to a stable solution of the tight-binding model is the amplitude that corresponds to the lowest-loss right eigenstate of the coupling matrix K.

To see why this is true, observe that $\lambda_j \cos(\Gamma_j)$ is the real part of the eigenvalue corresponding to the amplitude A_j. In our dissipatively coupled system [2], this corresponds to the dissipation associated with the couplings. In the steady state, the gain must satisfy $\lambda_j \cos(\Gamma_j) + g = \chi$ for some j. If j corresponds to the lowest-loss right eigenstate, then $\lambda_k \cos(\Gamma_k) < \lambda_j \cos(\Gamma_j)$ for all $k \neq j$, and therefore all fixed points but the one corresponding to the lowest-loss right eigenstate will experience net loss.

On the other hand, if j does not correspond to the lowest-loss right eigenstate, then $\lambda_{\text{low}} \cos(\Gamma_{\text{low}}) > \lambda_j \cos(\Gamma_j)$, and the lowest-loss right eigenstate will experience net gain. The lowest-loss right eigenstate will grow until it saturates the gain, at which point it will suppress the other, higher-loss eigenstates. This argument, combined with our master equation simulations below, provide compelling evidence that the lowest-loss right eigenstate defined by the coupling matrix K is a stable fixed point of this tight-binding model.

One caveat to the above conclusions is that they only hold for sufficiently large values of the small signal gain g_0. In other words, the gain must be large enough for the laser to go above threshold. This occurs when $\chi < \lambda_{\text{low}} \cos(\Gamma_{\text{low}}) + g_0$. On the other hand, when $\chi > \lambda_{\text{low}} \cos(\Gamma_{\text{low}}) + g_0$, then we expect $\mathbf{A} = 0$ to be a stable solution.

From our analysis in this section, we expect the pulse pattern in our temporally mode-locked laser to correspond to the lowest-loss eigenstate of the coupling matrix K. However, while we expect the relative amplitudes and phases of the pulses to be fixed in this state, Eq. 10c predicts that the pulse pattern can acquire a global phase over time. From Eq. 10c we see that this phase is governed by the imaginary part of the eigenvalue, $\lambda_j \sin(\Gamma_j)$.

4.3 Master Equation Simulations

To check the analytical results of the last section, we directly simulate the modified master equation in Eq. 1 for both the NH-SSH domain wall and the Hatano-Nelson nascent skin mode studied in the main text. For these simulations we use the dimensionless parameters $g_0 = 4$, $\Delta_{\text{IM}} = 0.04$, $T_{\text{RT}} = 0.01$, $\omega_{\text{rep}} = 2\pi (64/T_{\text{RT}})$, $D_{\text{g}} \approx 2.5 \times 10^{-15}$, and $\gamma = 2.56 \times 10^{-5}$. The strengths of the coupling coefficients vary according to the model under study, and we set $\ell = \ell_{\text{base}} + \ell_{\text{coupling}}$, where $\ell_{\text{base}} = 0.04$ and ℓ_{coupling} equals the maximum sum of the coupling coefficients in any row of the coupling matrix that describes the model under study.
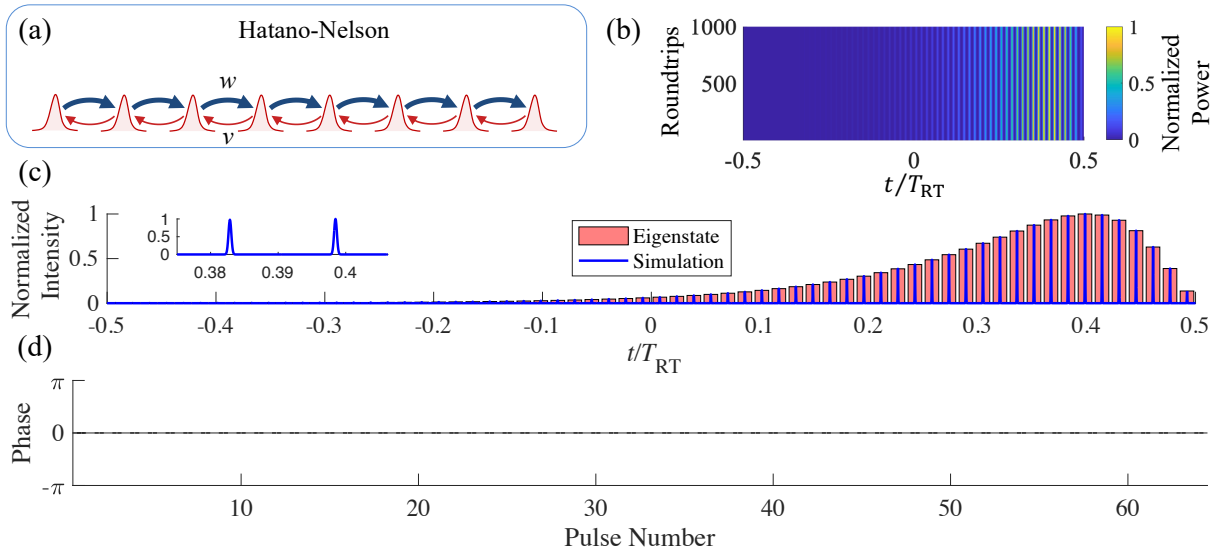
Figure 5: **Master Equation Simulation of the Hatano-Nelson Nascent Skin Mode.** (a) Schematic of the Hatano-Nelson model. (b) Heat map of the final 1000 roundtrips in our simulation. The pulses in the heat map are broadened for visibility. (c) Comparison between the simulated nascent skin mode and the lowest-loss right eigenstate defined by the couplings. (d) The phases at the peaks of the pulses are uniform through the lattice.

First, we simulate a boundary in a Hatano-Nelson lattice. We implement the Hatano-Nelson lattice shown in Fig. 5(a) with $w = 0.08$, $w/v = \sqrt{2}$, and the coupling between the first and final pulses in the lattice suppressed by a factor of 11.6. We initialize our simulation with Gaussian random noise ($\mu = 0$, $\sigma = 10^{-6}$) on both the real and imaginary parts of the field, and we inject noise distributed according to the same distribution into our simulation at the start of each roundtrip. We run our simulation for 10^5 roundtrips, the final 1000 of which are shown in Fig. 5(b). At this point, the simulation has reached steady state, and the pulse pattern in the simulation corresponds to the nascent skin mode predicted by the lowest-loss right eigenstate of the underlying lattice [Fig. 5(c)]. Note that, as expected, the pulse-to-pulse phases (as measured from the peaks of the pulses) are uniform [Fig. 5(d)].

We next repeat this simulation with a NH-SSH domain wall. This domain wall is shown in Fig. 6(a); we consider $w = 0.08$, $w/v = \sqrt{2}$, and $\kappa = (w + v)/2$. Here, we also find that the simulated steady state of the system corresponds to the lowest-loss right eigenstate of the model under consideration.
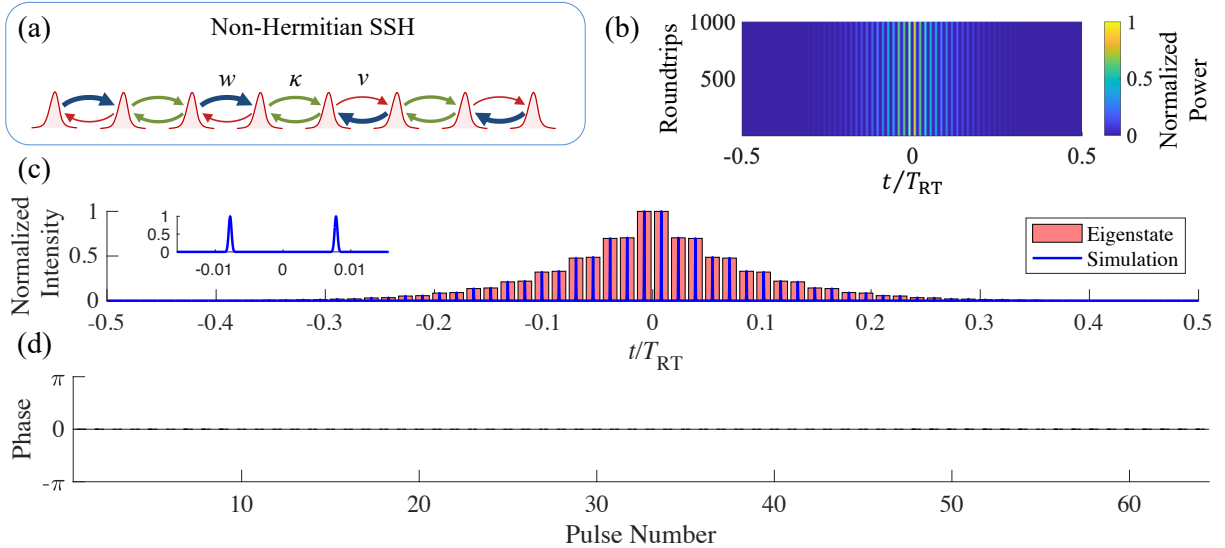
13

Figure 6: **Master Equation Simulation of the NH-SSH Domain Wall. (a)** Schematic of the NH-SSH domain wall. **(b)** Heat map of the final 1000 roundtrips in our simulation. The pulses in the heat map are broadened for visibility. **(c)** Comparison between the simulated domain wall skin mode and the lowest-loss right eigenstate defined by the couplings. **(d)** The phases at the peaks of the pulses are uniform through the lattice.

5 Lumped Element Simulations

As we mentioned in the Sec. 4.1, our topological temporally mode-locked laser operates beyond some of the assumptions that enter the derivation of our master equation. For this reason, here we perform lumped element simulations to confirm that the predictions of our master equation are reasonable beyond the assumptions of the model. The lumped element simulations in this section are adapted from simulations found in the literature [5].

5.1 Elements of the Lumped Element Simulations

Our lumped element simulations divide our temporally mode-locked laser into five elements, which are passive optical fiber, erbium-doped fiber, a filter, an intensity modulator, and intra-cavity couplings. Below we outline how we implement each of these elements.

5.1.1 Passive Fiber

We model the passive fiber in our simulation with the nonlinear Schrödinger equation

$$\frac{\partial A}{\partial z} + \frac{i\beta_2}{2}\frac{\partial^2 A}{\partial T^2} + \frac{1}{2}\alpha A = i\gamma \left|A\right|^2 A. \tag{12}$$

14

Here A is the field in the fiber, β_2 is the group velocity dispersion (GVD), α is the loss co-efficient, and γ is the nonlinear coefficient. In our simulations we consider dispersion shifted fiber with $\alpha = 0$ m^{-1}, $\beta_2 = -3.82 \times 10^{-9}$ ns^{2}m^{-1}, and $\gamma = 1.53 \times 10^{-3}$ W^{-1}m^{-1}. To speed up our simulation times, we consider only a short length of passive fiber ($L_{\mathrm{DSF}} = 2$ m) in our simulations. We simulate this fiber using the FFT to evaluate the derivative with respect to T and RK4 to propagate the field with respect to z.

5.1.2 Erbium-Doped Fiber

We model the EDFA in our simulation with a nonlinear Schrödinger equation that includes an additional gain term:

$$\frac{\partial A}{\partial z} + \frac{i}{2}\left(\beta_{2,\mathrm{EDFA}} + igT_2^2\right)\frac{\partial^2 A}{\partial T^2} - \frac{1}{2}\left(g - \alpha_{\mathrm{EDFA}}A\right) = i\gamma_{\mathrm{EDFA}}\left|A\right|^2 A. \tag{13a}$$

$$g = \frac{g_0 A}{1 + \frac{1}{P_{\mathrm{sat}}}\int_{T_{\mathrm{RT}}/2}^{T_{\mathrm{RT}}/2}\left|A\right|^2 dT} \tag{13b}$$

Here T_2 determines the gain bandwidth, g_0 is the small signal gain, and P_{sat} is the saturation power. Notice that our equation for the gain g explicitly assumes the slow gain saturation regime discussed in the main text. Assuming this simple form for the gain greatly simplifies our lumped element simulations.

For the erbium doped fiber, we use the following parameters: $\beta_{2,\mathrm{EDFA}} = -21.7 \times 10^{-9}$ ns^{2}m^{-1}, $\alpha_{\mathrm{EDFA}} = 0$ m^{-1}, $T_2 = 10^{-4}$ ns, and $P_{\mathrm{sat}} = 10^{-3}$ W. As we did for the dispersion shifted fiber, we consider only a short length of erbium doped fiber ($L_{\mathrm{EDF}} = 0.5$ m) in our simulations. Once again, we simulate the erbium doped fiber by using the FFT to evaluate the derivative with respect to T and RK4 to propagate the field with respect to z.

5.1.3 Filter

For the filter, we consider a Gaussian filter with the transfer function

$$H(f) = \alpha_{\mathrm{F}}\exp\left[-\frac{1}{2}\left(\frac{f}{B_0}\right)^2\right]. \tag{14}$$

Here α_{F} is the loss associated with the filter, and B_0 is the filter bandwidth. For our simulations we choose $\alpha_{\mathrm{F}} = 1$ and $B_0 = 400$ ns^{-1}.

5.1.4 Intensity Modulator

We model the intensity modulator in our simulations with the equation

$$T_{\mathrm{IM}}(t) = \alpha_{\mathrm{m}}\cos\left(\frac{\pi}{4}\left[\Delta_{\mathrm{m}}\cos(\omega_{\mathrm{m}}t) + \frac{2V_{\mathrm{B}}}{V_\pi}\right]\right). \tag{15}$$

15

Here α_m accounts for the loss in the intensity modulator, Δ_m is the modulation depth, V_B is the bias voltage applied to the modulator, V_π is the voltage needed to shift the modulator bias by π, and ω_m is the angular frequency associated with the repetition period T_{RT}/N, where N is the number of pulses in the laser cavity. For our simulations we choose $\alpha_m = 1$, $\Delta_m = 0.2$, and $V_B/V_\pi = 0.5$.

5.1.5 Intracavity Couplings

For a laser with N pulses, we implement the intracavity couplings by decomposing the field in the laser into N segements of equal length, where each segment contains a single pulse. We treat these segments as the elements of a vector and operate on them with the coupling matrix K that describes the dissipative couplings of the model under study. At the same time, we also introduce coupling losses into each of these segments. We then combine the N segments and add them to the original laser field.
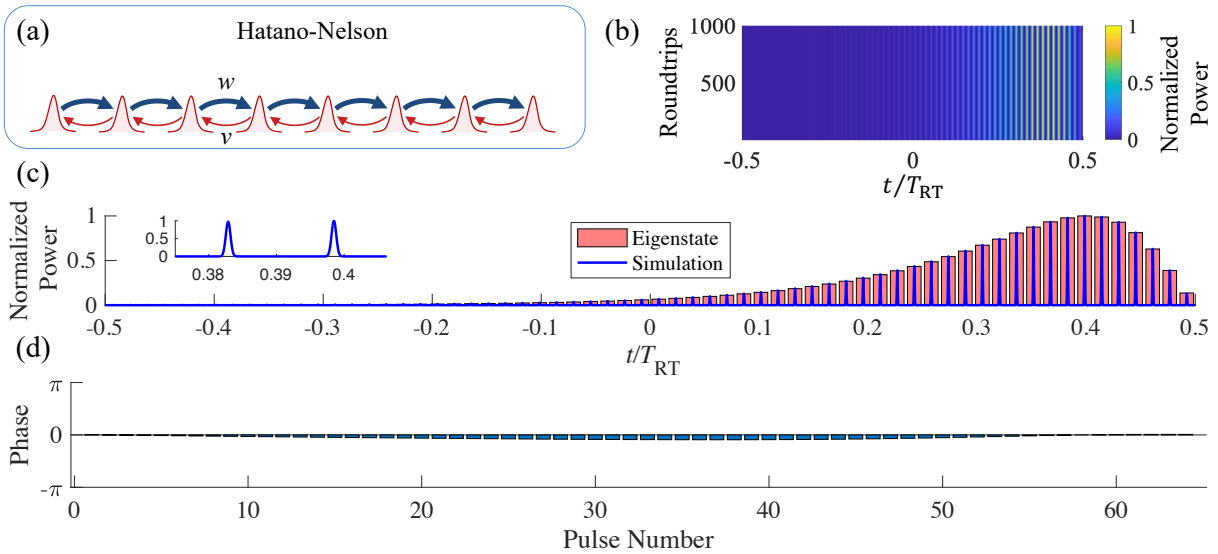

Figure 7: **Low Power Lumped Element Simulation of the Hatano-Nelson Model.** **(a)** Schematic of the Hatano-Nelson model. **(b)** Heat map of the final 1000 roundtrips in our simulation. The pulses in the heat map are broadened for visibility. **(c)** The amplitudes of the simulated pulse pattern are in excellent agreement with the predictions of the master equation. **(d)** A small degree of nonuniformity in the pulse-to-pulse phases arises because of the finite Kerr nonlinearity.

16

5.2 Lumped Element Simulations at Lower Power

We first perform our lumped element simulations in the "low power" regime, which we define to be the regime for which the Kerr nonlinearity does not appear to have a major effect on the simulation result. As we shall see, at higher powers, the Kerr nonlinearity appears capable of substantially changing the state of our temporally mode-locked laser relative to the predictions of our master equation. For the following simulations, we use a small signal gain of $g_0 = 2.0 \text{ m}^{-1}$.

As our first simulation in the low power regime, we program the couplings in our simulation to implement a Hatano-Nelson lattice with $w/v = \sqrt{2}$ and with the couplings at the boundary suppressed by a factor of 11.6. Here, and for all the simulations in this section, we initialize the field in our simulations with noise distributed according to $\mathcal{N}(0, 10^{-9}) + i\mathcal{N}(0, 10^{-9}) \text{ W}^{1/2}$, and, on each roundtrip of the simulation, we inject noise distributed according to the same distribution. We show the results of our simulation in Fig. 7. We observe that the results of our lumped element simulation are very similar to the results of the master equation simulation in Fig. 5. The one notable difference is that the pulse-to-pulse phases are no longer uniform in the lumped element simulation. This nonuniformity is a direct consequence of the presence of the Kerr nonlinearity in our lumped element simulation, and we have verified that, if we set $\gamma = \gamma_{EDFA} = 0 \text{ W}^{-1}\text{m}^{-1}$, this phase nonuniformity disappears.

We next perform a lumped element simulation for a NH-SSH domain wall with $w/v = \sqrt{2}$ and $\kappa = (w + v)/2$. These results are shown in Fig. 8. Once again, we find that, except for small deviations in the pulse-to-pulse phases that result from the finite Kerr nonlinearity, our lumped element simulation exhibits excellent agreement with the predictions of our master equation.

5.3 Lumped Element Simulations at Higher Power

We next repeat the simulations from the previous section at higher powers, where the Kerr nonlinearity has a substantial impact on the dynamics of the laser. For these simulations, we use a small signal gain of $g_0 = 7.0 \text{ m}^{-1}$.

We first repeat our simulation of the Hatano-Nelson lattice with $w/v = \sqrt{2}$ and the coupling reduced at the boundary by a factor of 11.6. The results of this simulation are shown in Fig. 9. Now we find that the simulated steady state pulse pattern is substantially broader than the prediction of our master equation [Fig. 5(c)]. It is evident from Fig. 9(d) that the Kerr nonlinearity gives rise to a substantial nonlinear phase shift at this higher power, and we believe that this nonlinear phase shift is responsible for broadening the observed pulse pattern.

Next, we repeat the simulation of the NH-SSH domain wall with $w/v = \sqrt{2}$ and $\kappa = (w + v)/2$. The results of this simulation are shown in Fig. 10. Once again, we find that the pulse pattern in the laser is now substantially broader than what we would expect from the prediction of our master equation [Fig. 6(c)]. This broadening appears to be a result of the substantial nonlinear phase shift produced by the Kerr nonlinearity [Fig. 10(d)].
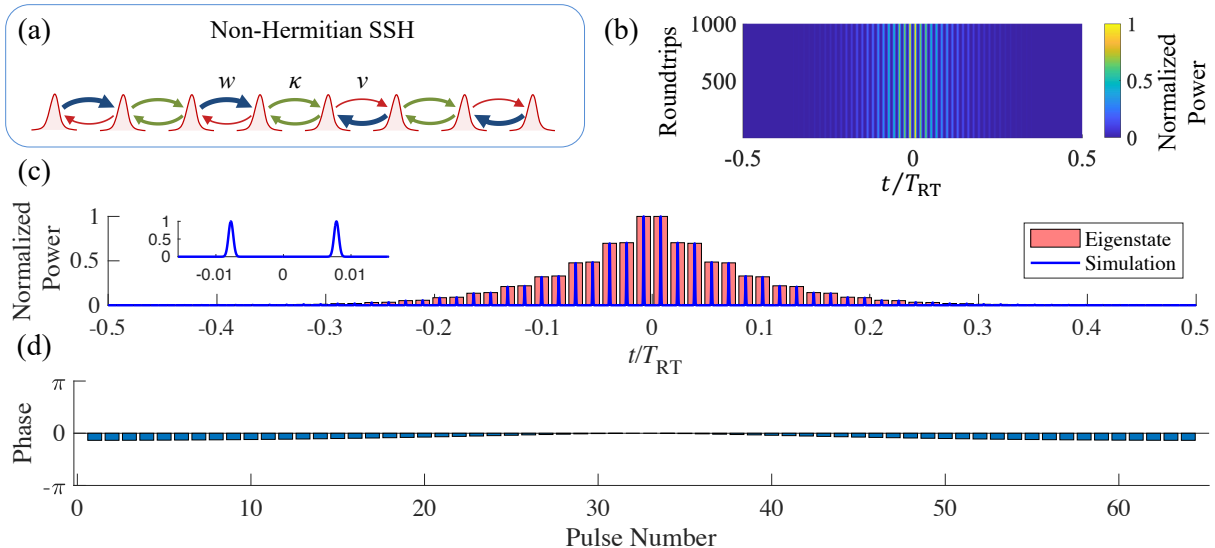
Figure 8: **Low Power Lumped Element Simulation of the NH-SSH Domain Wall.**
(a) Schematic of the NH-SSH domain wall. **(b)** Heat map of the final 1000 roundtrips in our simulation. The pulses in the heat map are broadened for visibility. **(c)** The amplitudes of the simulated pulse pattern are in excellent agreement with the predictions of the master equation. **(d)** A small degree of nonuniformity in the pulse-to-pulse phases arises because of the finite Kerr nonlinearity.

6 Robustness of the Hatano-Nelson Model

Here, we elaborate on the robustness measurements presented in the main text. We first present additional measurements for different realizations of disorder both in the topological, Hatano-Nelson lattice and in the trivial lattice. Then, we provide concrete localization metrics for the non-Hermitian lattices considered in this work, and we establish that the Hatano-Nelson model's sensitivity to the boundary conditions provides sufficient evidence of robustness against disorder-induced localization. Finally, we present simulations of larger lattices to account for finite size effects that can occur in our laser.

6.1 Additional Measurements

In Fig. 11 we present states measured at the output of our topological temporally mode-locked laser for a Hatano-Nelson lattice with four different realizations of non-Hermitian coupling disorder. As in the main text, we consider a Hatano-Nelson lattice with $w/v = 4$ and disorder nominally distributed according to $\mathrm{Unif}(0, 0.2w)$. In the presence of periodic boundary conditions [Fig. 11(a-d)], we observe that the measured state of the laser is distributed throughout the lattice for each realization of disorder. However, when we introduce boundaries at the edges
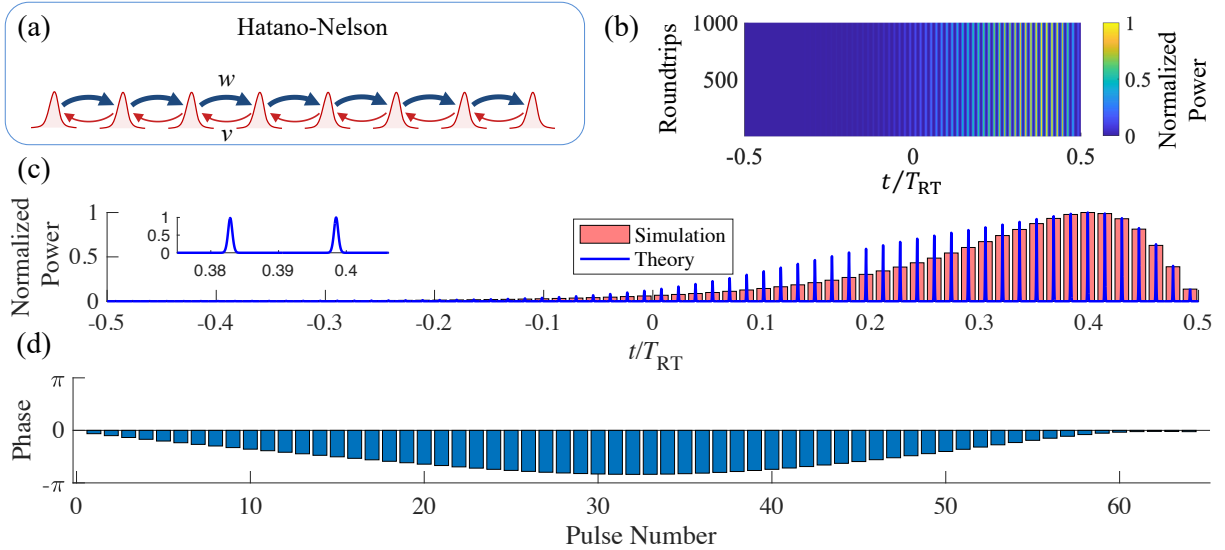
18

Figure 9: **Higher Power Lumped Element Simulation of the Hatano-Nelson Model.**
(a) Schematic of the Hatano-Nelson model. (b) Heat map of the final 1000 roundtrips in our simulation. The pulses in the heat map are broadened for visibility. (c) The steady state pulse pattern is substantially broadened relative to the prediction of the master equation. (d) The phases of the pulses exhibit a substantial nonlinear phase shift.

of the Hatano-Nelson lattices [Fig. 11(e-h)], we observe that nascent skin modes form near the boundaries of each Hatano-Nelson lattice. As we discussed in the main text, these nascent skin modes precede the occurrence of the non-Hermitian skin effect (NHSE) in the case of perfect open boundary conditions [6]. The NHSE guarantees the existence of a topological winding number in the lattice with periodic boundary conditions and provides experimental evidence for the claim that the robustness of the Hatano-Nelson model has a topological origin [7].

In Fig. 12, we show additional measurements of the state in our temporally mode-locked laser for the case of a disordered trivial lattice ($w/v = 1$). With periodic boundary conditions [Fig. 12(a-d)], the state observed in our laser in general appears not to be spread throughout the lattice. Moreover, in the presence of a boundary [Fig. 12(e-h)], the observed state generally appears almost identical to the state with periodic boundary conditions. This lack of sensitivity to the boundary conditions suggests that the trivial lattice enters a localized phase.

The one exception to the general trend in Fig. 12 is the states measured in Fig. 12(d,h). Here, in the presence of periodic boundary conditions, the state appears to be spread across the lattice, while in the presence of the boundary, the state looks substantially different (although it does not form a nascent skin mode). It is believed that this exception is the result of finite size effects in our laser's synthetic temporal lattice. We examine the consequences of these finite size effects in the next subsection.
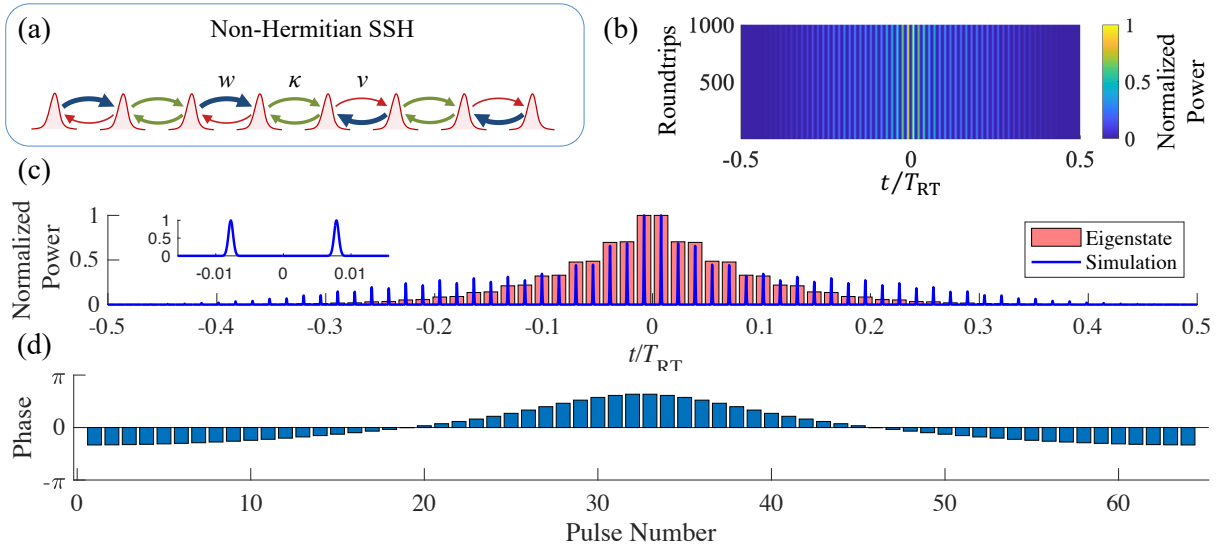
19

Figure 10: **Higher Power Lumped Element Simulation of the NH-SSH Domain Wall.**
(**a**) Schematic of the NH-SSH domain wall. (**b**) Heat map of the final 1000 roundtrips in our simulation. The pulses in the heat map are broadened for visibility. (**c**) The pulse pattern in the steady state is substantially broadened relative to the predictions of our master equation. (**d**) The phases of the pulses on the final roundtrip of the simulation, which reveal the presence of a substantial nonlinear phase shift.

6.2 Alternative Metric of Localization and Finite Size Effects

Above, and in the main text, we noted the sensitivity of the observed state in the Hatano-Nelson lattice to the boundary conditions is a sign of robustness against disorder-induced localization [8, 9]. Here, we provide another definition of localization, and we show that the Hatano-Nelson lattice studied in the main text appears to satisfy this definition, while the trivial lattice does not. We then show that this alternative definition of localization is consistent with the sensitivity to the boundary conditions used to claim robustness in our experiments.

We base our alternative metric of localization on the work of Hatano and Nelson [9]. We first recall that, in non-Hermitian quantum mechanics, the right and left eigenstates of a tight-binding Hamiltonian may be written in a biorthogonal basis. In our case, this means that the right eigenvectors $\left|\psi_m^{\mathrm{R}}\right\rangle$ and the left eigenvectors $\left\langle\psi_n^{\mathrm{L}}\right|$ satisfy the relationship

$$\left\langle\psi_n^{\mathrm{L}}\middle|\psi_m^{\mathrm{R}}\right\rangle = \delta_{mn}. \tag{16}$$

To define a localization metric in terms of $\left|\psi_m^{\mathrm{R}}\right\rangle$ and $\left\langle\psi_n^{\mathrm{L}}\right|$, we note that the density distribution in such a non-Hermitian quantum mechanical system is given by [9]
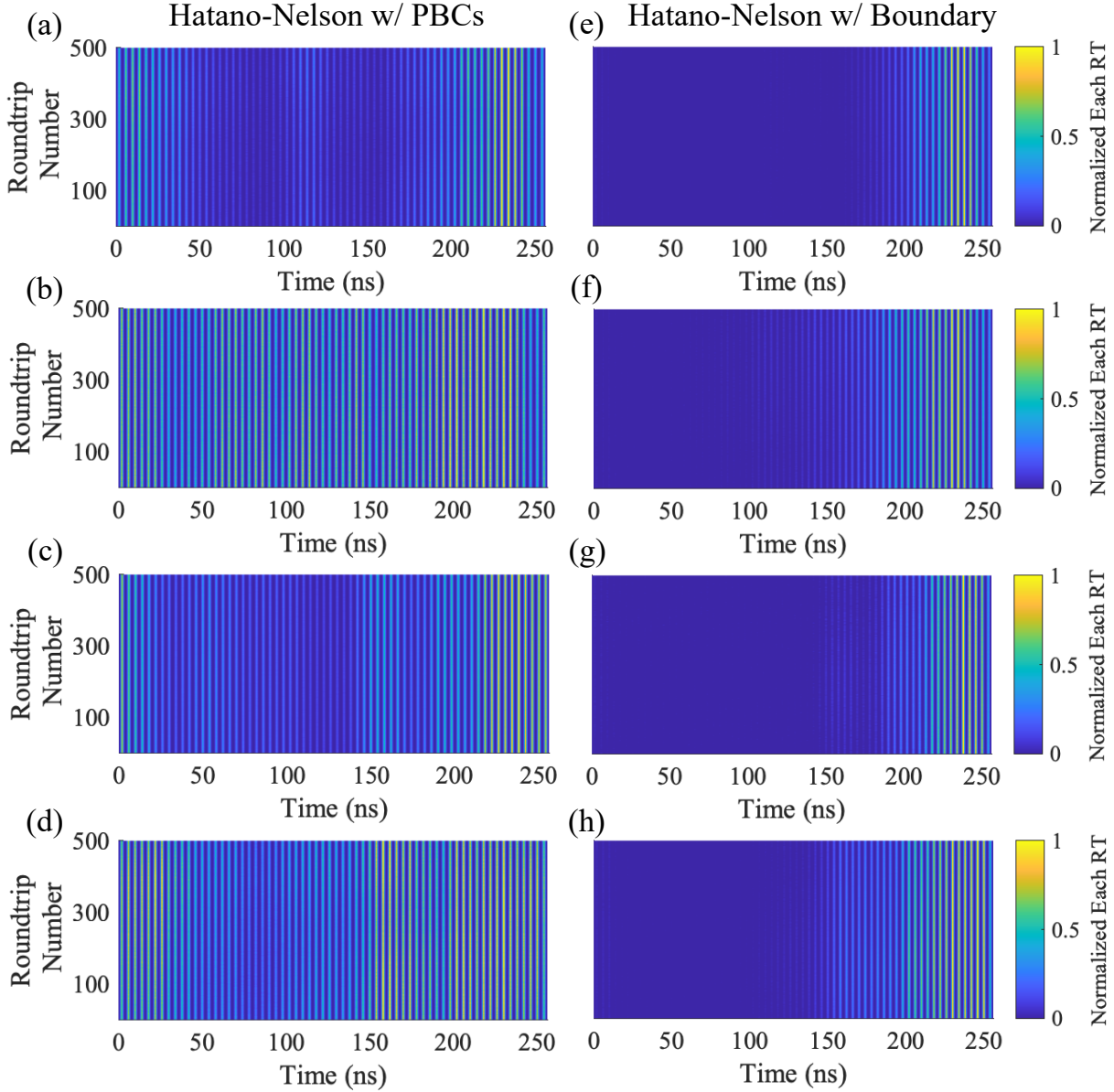
Figure 11: **Additional Measurements of Disordered Hatano-Nelson Lattices.** **(a-d)** Measured states in our topological temporally mode-locked laser for Hatano-Nelson couplings with periodic boundary conditions and different realization of disordered. **(e-h)** The states measured after introducing a boundary in the lattices. In all plots, the pulses are broadened for visibility.
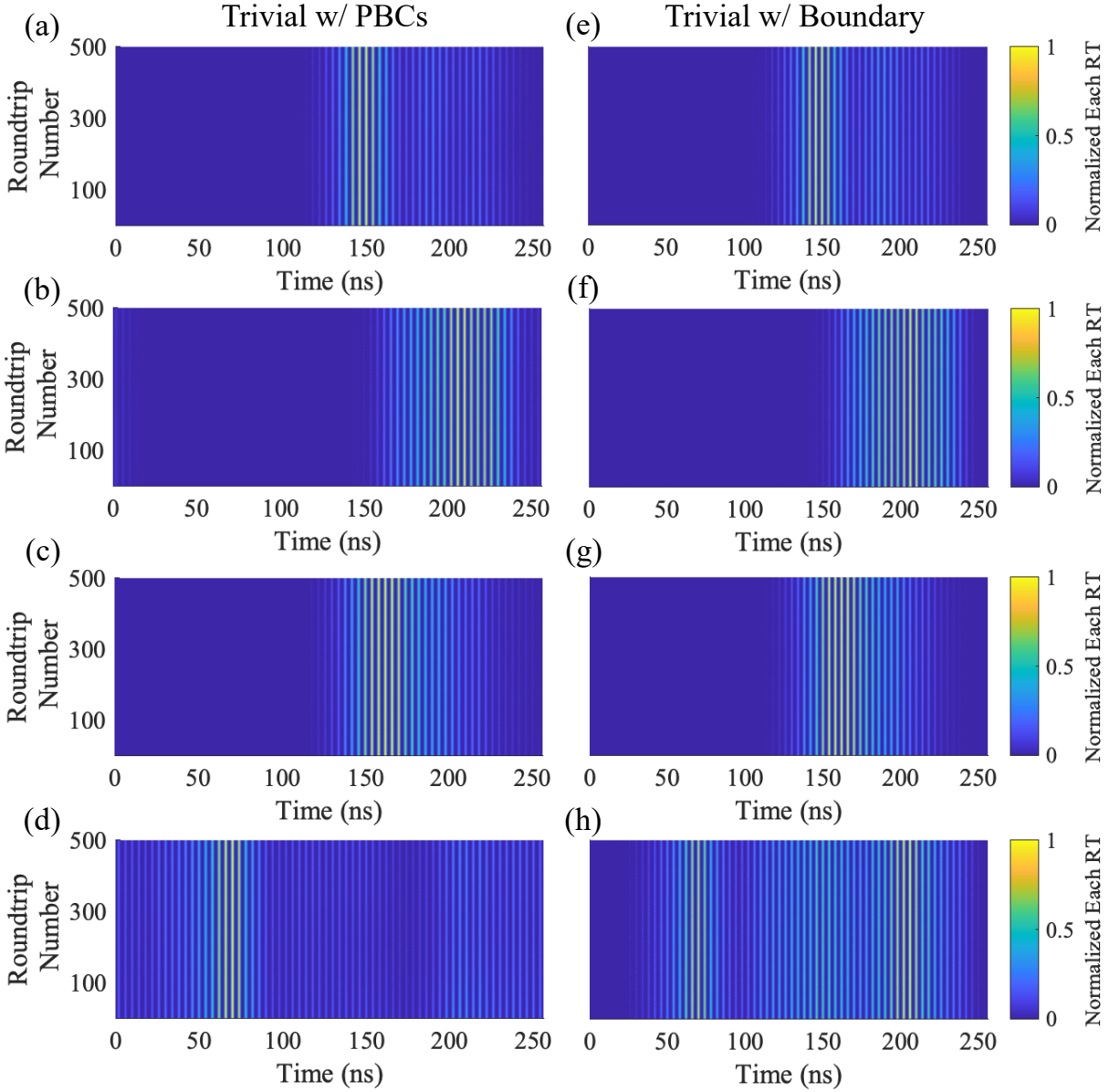
Figure 12: **Additional Measurements of Disordered Trivial Lattices. (a-d)** Measured states in our temporally mode-locked laser for different realizations of non-Hermitian coupling disorder in a trivial lattice with periodic boundary conditions. **(e-h)** The states measured after introducing a boundary in the lattices. In each case, the pulses are broadened for visibility.
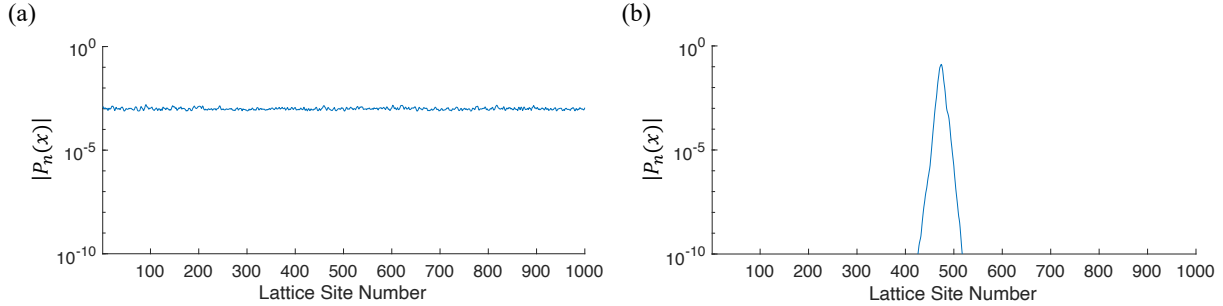
(a)

(b)

Figure 13: **Plot of** $|P_n(x)|$ **for Delocalized and Localized Lattices.** **(a)** Plot of the quantity $|P_n(x)|$ for a delocalized Hatano-Nelson lattice with periodic boundary conditions. **(b)** Plot of the quantity $|P_n(x)|$ for a localized trivial lattice with periodic boundary conditions.

$$P_n(x) = \sum_i^N \langle \psi_n^L | x_i \rangle \langle x_i | \psi_n^R \rangle | x_i \rangle, \tag{17}$$

and therefore, from a physical perspective, $P_n(x)$ is the relevant quantity to consider when discussing the delocalized phase of the Hatano-Nelson model.

In Fig. 13, we plot the quantity $|P_n(x)|$ for the lowest-loss states of a Hatano-Nelson lattice ($w/v = 4$) and of a trivial lattice ($w/v = 1$). Both lattices contain 1000 sites and have additional non-Hermitian coupling disorder distributed according to $\mathrm{Unif}(0, 0.2w)$. Despite the disorder, we observe that $|P_n(x)|$ remains quite uniform across the Hatano-Nelson lattice [Fig. 13(a)], which indicates that the state of the Hatano-Nelson lattice is delocalized. In contrast, we see that $|P_n(x)|$ in the trivial lattice is strongly localized. This suggests that the lowest-loss state of the trivial lattice enters a localized phase in the presence of the coupling disorder.

The flatness of $|P_n(x)|$ in the delocalized phase motivates us to define a generalized inverse participation ratio (IPR) to measure the delocalization of our non-Hermitian lattices:

$$\mathcal{L} = \sum_i^N \left| \langle \psi_n^L | x_i \rangle \langle x_i | \psi_n^R \rangle \right|^2. \tag{18}$$

Observe that $\mathcal{L}$ reduces to the conventional IPR in the case of a Hermitian lattice. If $|P_n(x)|$ remains roughly uniform throughout the lattice in the presence of disorder, then we expect that $\log_{N \to \infty} \mathcal{L} = 0$, where N is the size of the lattice.

In Fig. 14(a), we consider a Hatano-Nelson lattice with $w/v = 4$ and coupling disorder distributed according to $\mathrm{Unif}(0, 0.2w)$. We plot the average value of $\mathcal{L}$ over 1000 realizations of disorder for the lowest-loss state of the Hatano-Nelson lattice as a function of the lattice size, and we observe that $\mathcal{L}$ decreases as $1/N$. This behavior confirms that the lowest-loss state of the Hatano-Nelson lattice remains in a delocalized phase in the presence of this level of non-Hermitian coupling disorder. A similar simulation for the corresponding trivial lattice
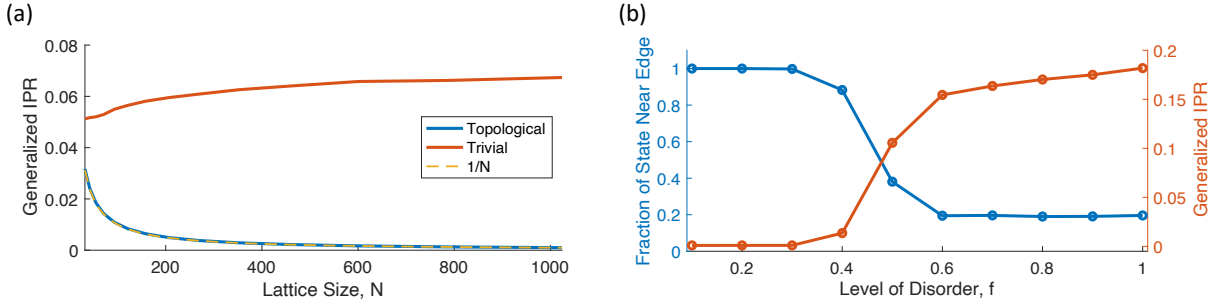
23

Figure 14: **Finite Size Effects or Relationship Between Localization Metrics.** **(a)** Average generalized inverse participation ratios (IPRs) plotted as a function of lattice size for the lowest-loss state of Hatano-Nelson lattices and trivial lattices with coupling disorder. The average generalized IPR of the Hatano-Nelson lattices is fit well by $1/N$, where N is the lattice size. **(b)** The average generalized IPR plotted as a function of disorder, as well as the fraction of the state that lies in the rightmost 20% of a Hatano-Nelson lattice with coupling disorder drawn from $\mathrm{Unif}(0, fw)$.

($w/v = 1$) shows that the average value of $\mathcal{L}$ increases as a function of N. This indicates that the trivial lattice enters a localized phase in the presence of disorder, and allows us to conclude that the measurements in Fig. 12(d,h) were the result of finite size effects.

Plotting $\mathcal{L}$ as a function of the lattice size enables us to conclude that the lowest-loss state of the Hatano-Nelson lattice remains in a delocalized phase for the level of disorder studied in our experiments. However, in practice, we do not have access to $\mathcal{L}$ because, in experiment, we measure the quantity $\sum_i^N \left| \langle x_i | \psi_n^R \rangle \right|^2 |x_i\rangle$. For this reason, we rely on the appearance of nascent skin modes to infer that the Hatano-Nelson lattice remains in a delocalized phase.

In Fig. 14(b), we provide evidence that $\mathcal{L}$ is correlated to the occurrence of the NHSE. Here, we plot the average fraction F_{20} of the lowest-loss state that lies in the rightmost 20% of a Hatano-Nelson lattice with $w/v = 4$, open boundary conditions, and coupling drawn from $\mathrm{Unif}(0, fw)$, where we define f as the level of disorder. We see that, for levels of disorder up to $f \approx 0.3$, F_{20} remains extremely close to unity, which suggests that the lowest-loss right eigenstate exhibits the NHSE in this regime. At higher levels of disorder F_{20} decreases rapidly to $\sim 1/5$, which is what we would expect if the lowest-loss state were randomly distributed in the lattice.

Along with F_{20}, in Fig. 14(b) we also plot the average generalized IPR $\mathcal{L}$ for the corresponding Hatano-Nelson lattices with periodic boundary conditions. We observe that $\mathcal{L}$ remains relatively flat up to levels of disorder of $f \approx 0.3$. For greater levels of disorder, $\mathcal{L}$ increases rapidly before beginning to level off at larger values of f. The increase in $\mathcal{L}$ indicates that the lowest-loss state of the Hatano-Nelson lattice is entering a localized phase.

The correlation between the drop in F_{20} and the rise in $\mathcal{L}$ leads us to conclude that the appearance of the NHSE is a reliable signature that the lowest-loss state of the Hatano-Nelson

24

lattice with periodic boundary conditions is in a delocalized phase. From this, we conclude that the nascent skin modes observed in our topological temporally mode-locked laser provide sufficient evidence to conclude that the Hatano-Nelson lattice implemented in our laser is robust against disorder-induced localization.

7   Potential for Robust Frequency Combs

In the main text, we discussed how temporal mode-locking can stabilize both the relative amplitudes and phases of the pulse train in a harmonically mode-locked laser. Stabilizing the relative phases of the pulses is important from a technological perspective because it can make a harmonically mode-locked laser suitable for frequency domain applications [10]. In this section, we use lumped element simulations to explore how topological temporal mode-locking can stabilize the pulse-to-pulse phases of a harmonically mode-locked laser in a way that is robust against disorder.

First, to emphasize the role that temporal mode-locking plays in phase locking the pulses of a harmonically mode-locked laser, we simulate a traditional, harmonically mode-locked laser without intracavity couplings. For this simulation, we use the same parameters that were used in Sec. 5, and we use $g_0 = 7.0$ m^{-1}. Also, as in Sec. 5, we initialize the field in our simulation with noise distributed according to $\mathcal{N}\left(0, 10^{-9}\right) + i\mathcal{N}\left(0, 10^{-9}\right)$ W$^{1/2}$, and, on each roundtrip of the simulation, we inject noise distributed according to the same distribution. We let the simulation to reach steady state, and then we compute the Fourier transform of the final 1000 roundtrips in the steady state. We show our results in Fig. 15. As expected, we see that the amplitudes of the mode-locked pulses are uniform [Fig. 15(a)] but that the phases are random [Fig. 15(b)] due to the presence of noise in the simulation. As a result, the comb lines in the power spectral density have a random nature [Fig. 15(c)], which makes such a laser unsuitable for frequency domain applications.

Our simulation results change dramatically once we include temporal mode-locking. In Fig. 16 and Fig. 18, we simulate temporally mode-locked lasers that implement a Hatano-Nelson lattice with $w/v = 10$ and a trivial lattice, respectively. For each lattice, we consider 128 pulses and $g_0 = 2.0$ m^{-1}. In each case, we see that the pulse-to-pulse phases are now constant across the pulse trains. Together, these constant phases and amplitudes result in well defined, equally spaced comb lines. In sharp contrast to the laser without temporal mode-locking, the well-defined frequency combs suggest that these lasers could be suitable for frequency domain applications.

While both the topological Hatano-Nelson lattice and the trivial lattice can stabilize the pulse-to-pulses phases in the absence of disorder, we expect that the robustness of the topological Hatano-Nelson lattice will also make the frequency comb in Fig. 16(c) robust against disorder. In contrast, we expect that the trivial comb in Fig. 18(c) will be sensitive to disorder due to the lack of an Anderson transition in trivial one-dimensional lattices.

To verify this prediction, we simulate the Hatano-Nelson and trivial lattices with addi-
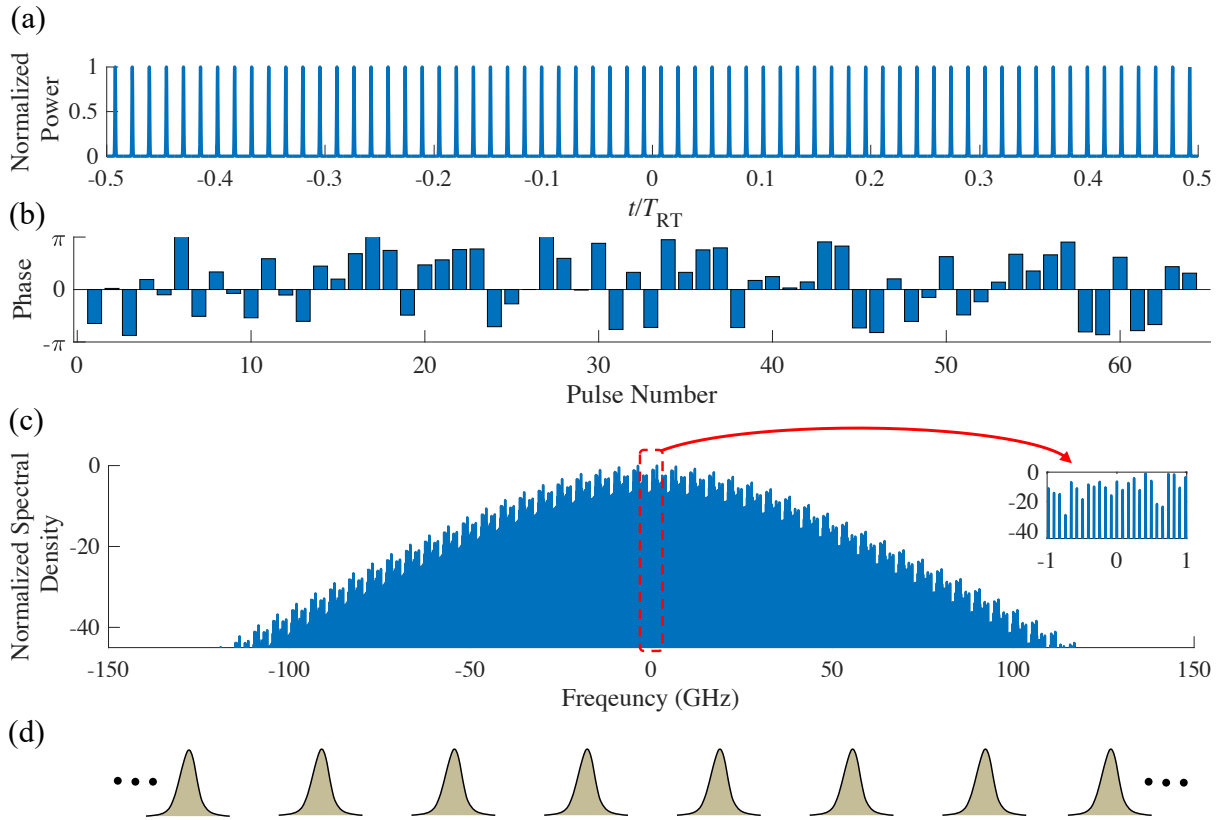
Figure 15: **Harmonically Mode-Locked Laser without Temporal Mode-Locking. (a)** The amplitudes in the harmonically mode-locked laser are uniform. **(b)** In the absence of temporal mode-locking, the phase of the pulses can drift randomly with respect to one another. **(c)** The randomness in the resulting frequency comb makes this laser unsuitable for frequency domain applications. **(d)** The pulses in a harmonically mode-locked laser without intracavity couplings.
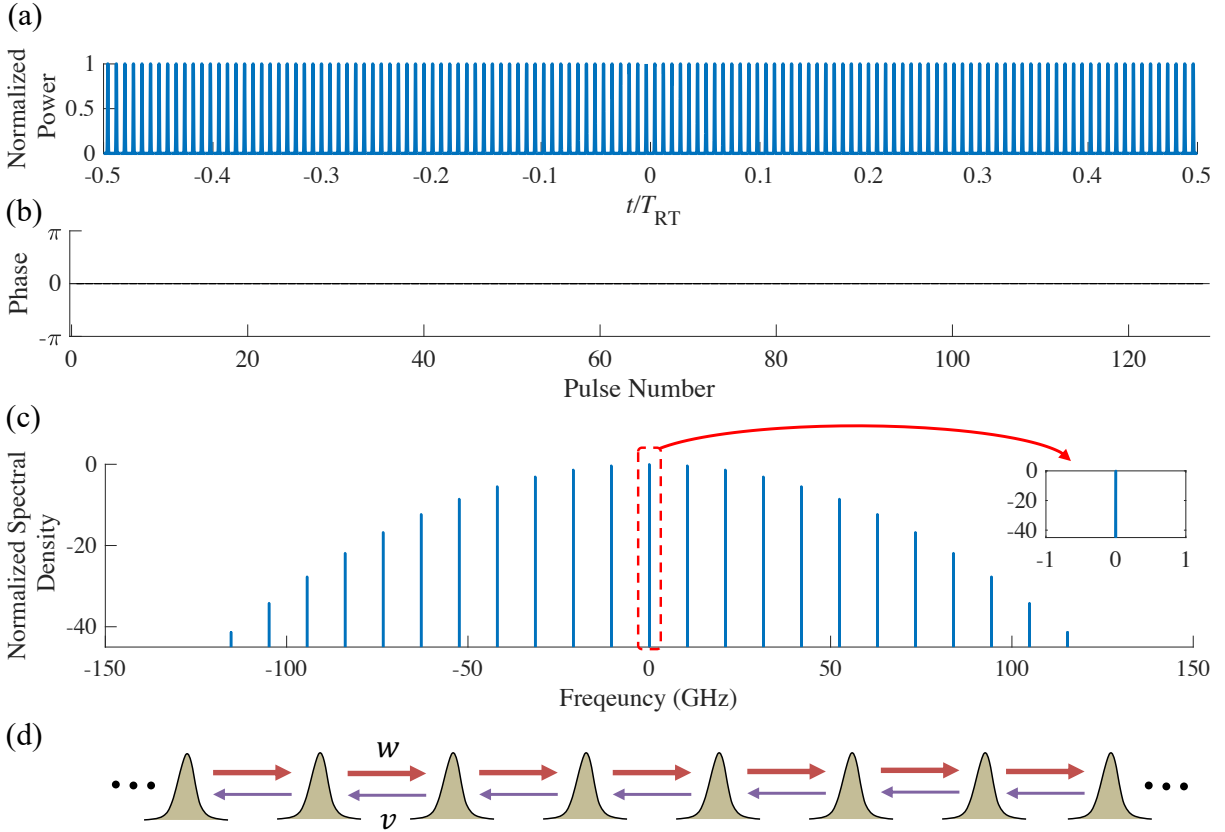
26

Figure 16: **Temporal Mode-Locking with Hatano-Nelson Couplings and No Disorder. (a-c)** Without disorder, the topological temporally mode-locked laser exhibits uniform pulse amplitudes, uniform pulse-to-pulse phases, and a well-defined frequency comb. **(d)** Schematic of the Hatano-Nelson model without disorder.
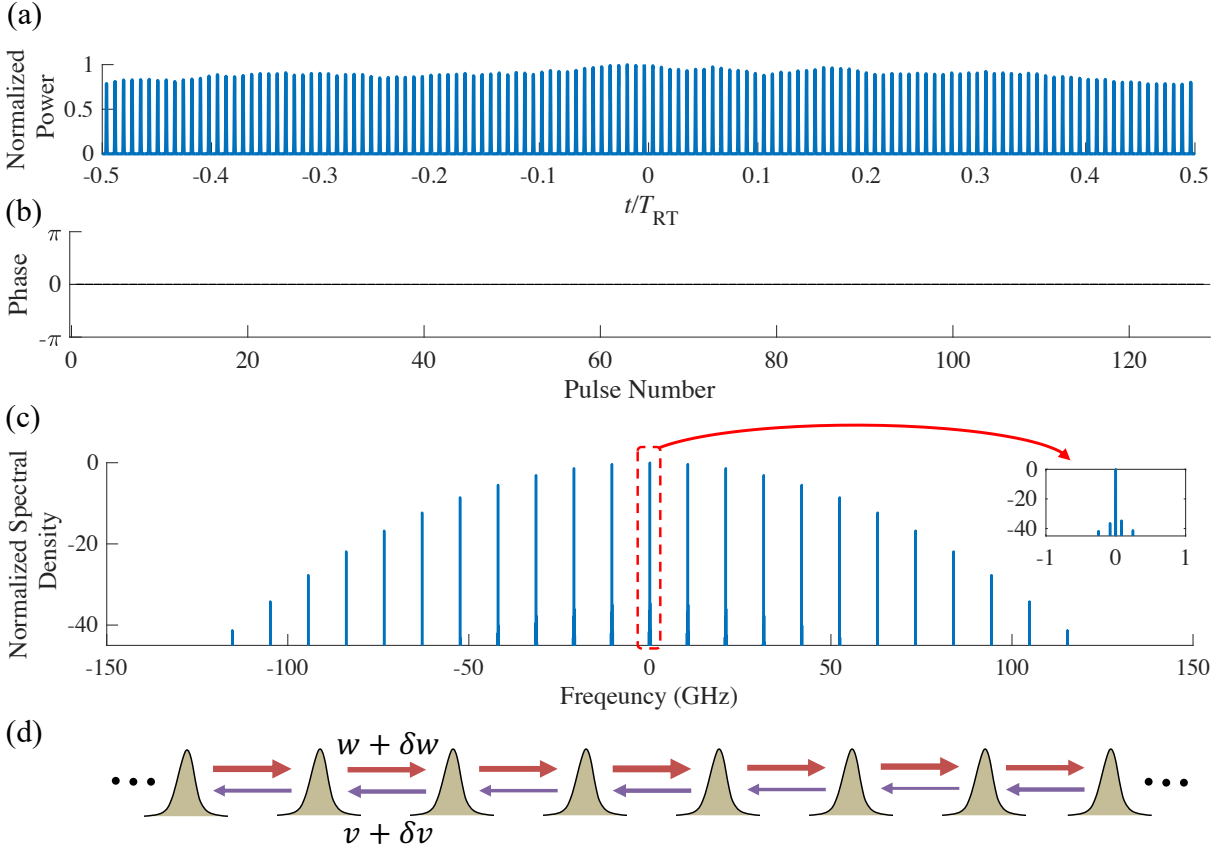
Figure 17: **Temporal Mode-Locking with Hatano-Nelson Couplings and Coupling Strength Disorder.** **(a-c)** With the addition of coupling noise, the pulse train is only mildly perturbed, and secondary comb lines remain well suppressed. **(d)** Schematic of the Hatano-Nelson model with disorder.
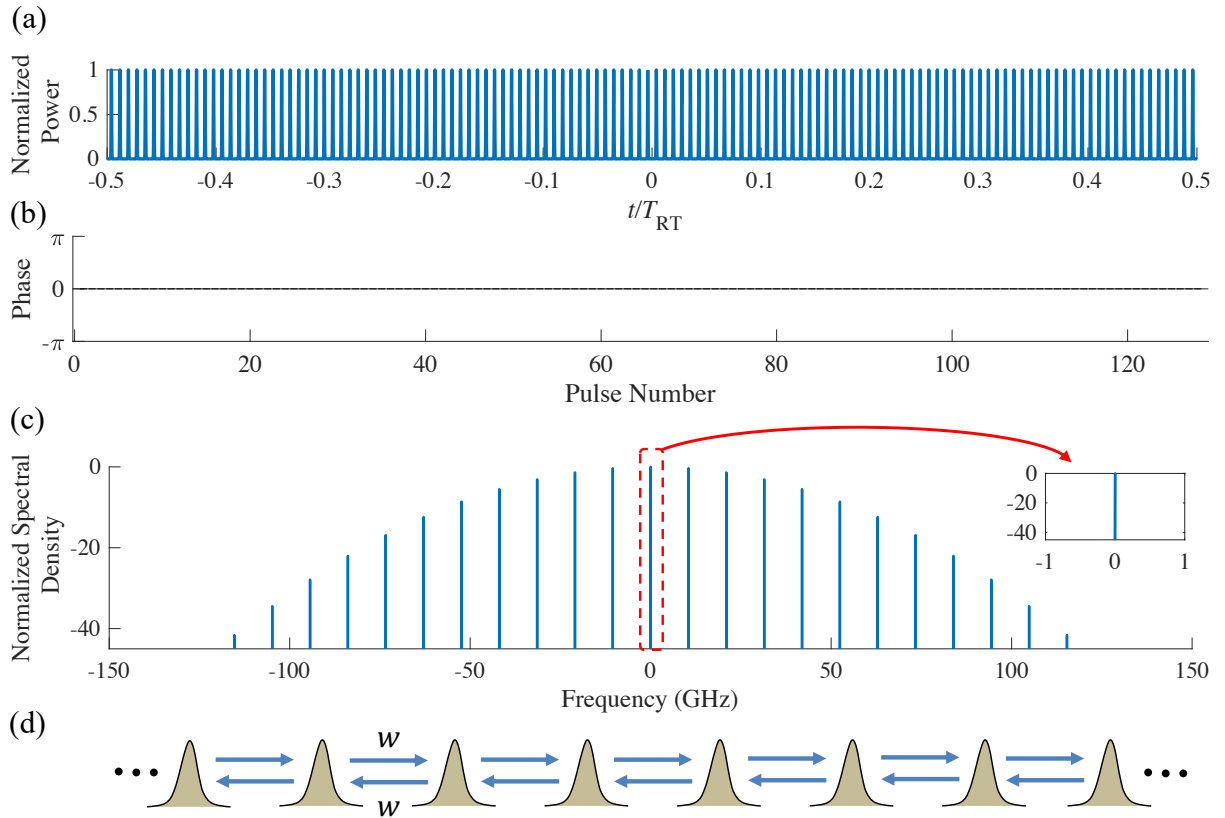
Figure 18: **Temporal Mode-Locking with Trivial Couplings and No Disorder. (a-c)** Without disorder, the trivial temporally mode-locked laser exhibits uniform pulse amplitudes, uniform pulse-to-pulse phases, and a well-defined frequency comb. **(g)** Schematic of the trivial lattice without disorder.
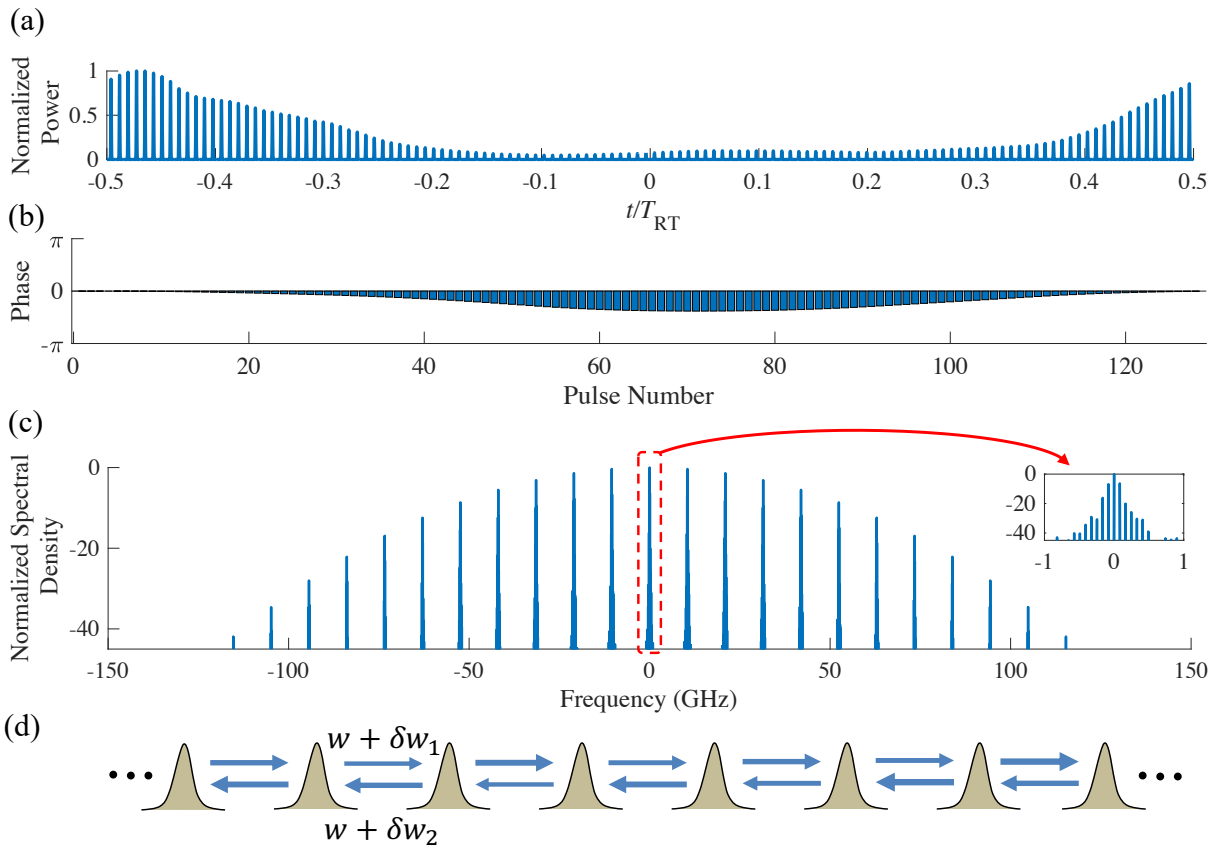
Figure 19: **Temporal Mode-Locking with Trivial Couplings and Coupling Strength Disorder. (a-c)** With coupling disorder, the pulse train is strongly distorted, and the secondary comb lines become prominent. **(d)** Schematic of the trivial lattice with disorder.

Figure 20: **Temporal Mode-Locking with Hatano-Nelson Couplings and Phase Disorder.**
(a) In the presence of coupling phase disorder, the pulse amplitudes in the topological temporally mode-locked laser are only slightly distorted. **(b)** The addition of coupling phase disorder introduces some inhomogeneity in the pulse-to-pulse phases. **(c)** Despite the coupling phase disorder, the secondary comb lines are still suppressed by over 10 dB relative to the primary comb lines. **(d)** Schematic of a topological Hatano-Nelson lattice with non-Hermitian coupling phase disorder.
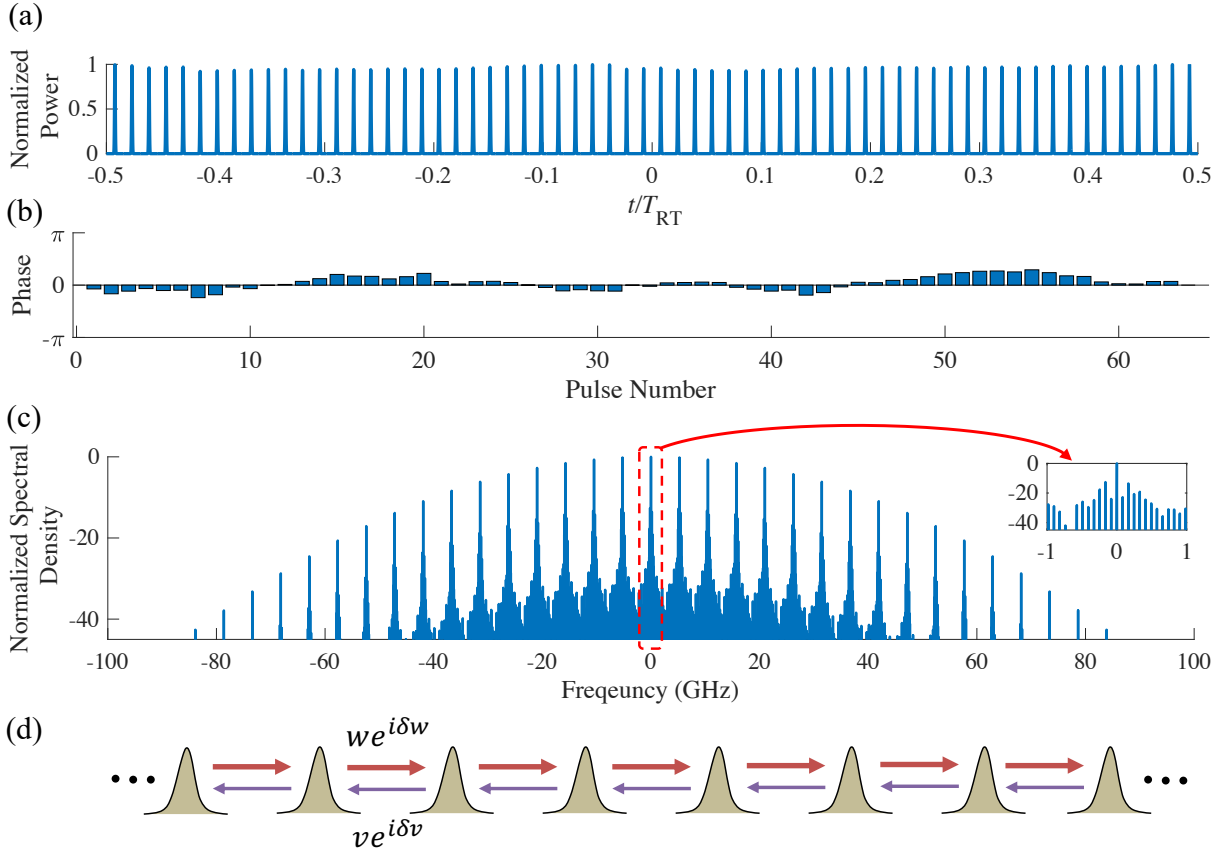
31

Figure 21: **Temporal Mode-Locking with Trivial Couplings and Phase Disorder. (a)** In the presence of coupling phase disorder, the pulse amplitudes in the trivial temporally mode-locked laser are substantially distorted. **(b)** The addition of coupling phase disorder introduces substantial inhomogeneity in the pulse-to-pulse phases. **(c)** Due to the coupling phase disorder, the next largest secondary comb lines are only suppressed by less than 2 dB relative to the primary comb lines. **(d)** Schematic of a trivial lattice with non-Hermitian coupling phase disorder.

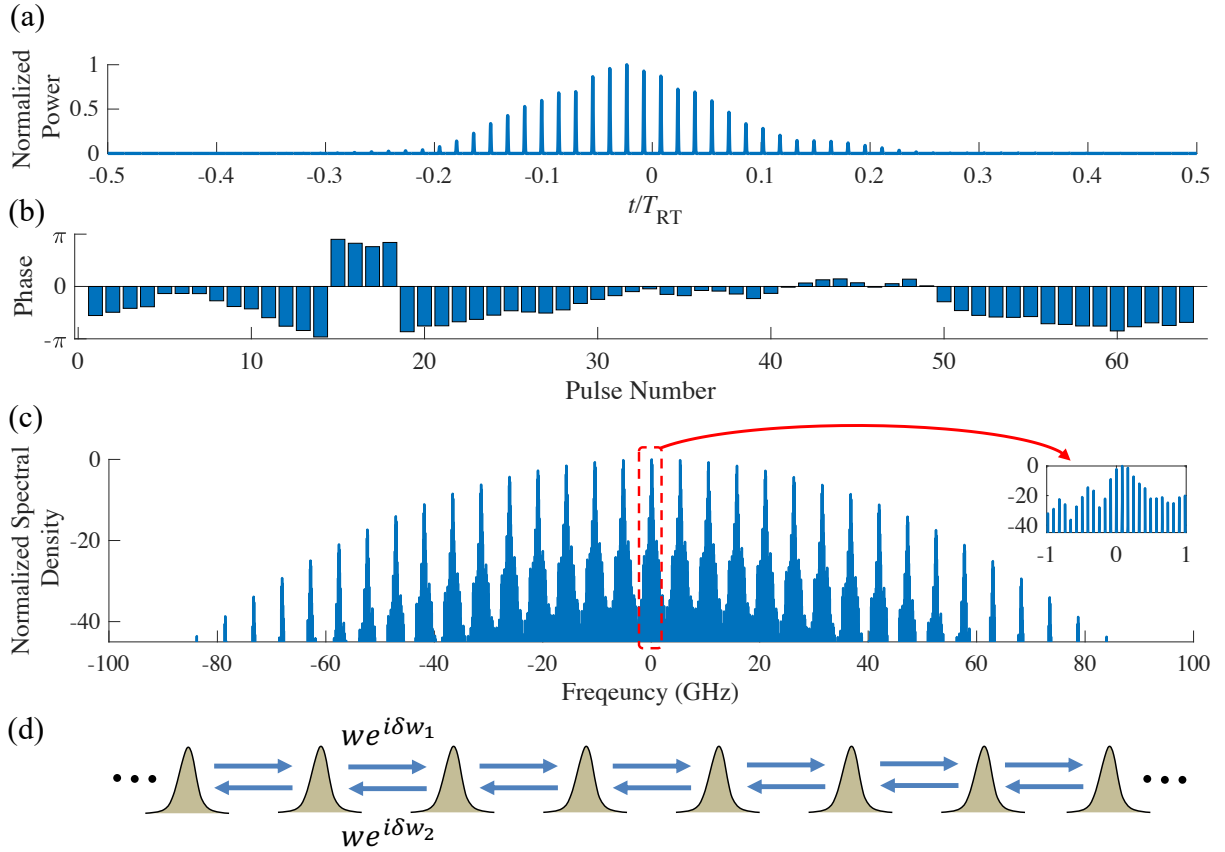tional non-Hermitian coupling disorder distributed according to $\mathrm{Unif}(0, 0.02w)$. Once again, we initialize the field in our simulation with noise distributed according to $\mathcal{N}\left(0, 10^{-9}\right) + i\mathcal{N}\left(0, 10^{-9}\right)$ $\mathrm{W}^{1/2}$, and we inject identically distributed noise on each roundtrip of the simulation. In the presence of the coupling disorder, we observe that the amplitudes and phases of the pulses in the topological Hatano-Nelson lattice remain largely uniform [Fig. 17(a,b)]. Zooming in on the central comb lines in the resulting frequency comb, we see that the nearest secondary comb line is still be suppressed by over 34 dB [Fig. 17(c)]. In contrast, the amplitudes and phases of the pulses in the trivial lattice are greatly altered by the disorder in the lattice [Fig. 19(a,b)]. As a result, when we zoom in on the central comb lines in the resulting frequency comb, we see that the nearest secondary comb line is suppressed by less than 7 dB [Fig. 19(c)]. Together, these results in Fig. 17 and Fig. 19 indicate that topological temporal mode-locking can offer a distinct advantage for building temporally mode-locked frequency combs over its trivial counterpart.

In addition to being robust against disorder in the coupling strengths, we also expect the Hatano-Nelson lattice implemented in our topological temporally mode-locked laser to be robust against disorder in the coupling phases. To illustrate this, we perform additional simulations with random non-Hermitian coupling phase disorder. Here we consider random phases distributed according to $2\pi\mathcal{N}(0, 1/32)$, so that we multiply each direction of each coupling by a term of the form $e^{i\zeta}$, where ζ is the random phase.

The static coupling phase disorder considered here effectively simulates low-frequency pulse-to-pulse phase noise. Therefore, these simulations demonstrate the robustness of our topological frequency comb against low-frequency phase noise.

We perform these simulations using the same parameters as in the Sec. 5. We use $g_0 = 2$ m^{-1}, and we simulate lattices with 64 pulses. As in our other simulations, we initialize the field with noise distributed according to $\mathcal{N}(0, 10^{-9}) + i\mathcal{N}(0, 10^{-9})$ W$^{1/2}$, and we inject identically distributed noise on each roundtrip of the simulation.

In Fig. 20 we present a simulation of a topological Hatano-Nelson lattice with $w/v = 10$ and phase noise. In the absence of disorder, we expect to observe a uniform pulse train with uniform phases, as we observed in Fig. 16(a,b). In the Hatano-Nelson lattice, we observe that the steady-state amplitudes remain largely uniform in the presence of disorder. Meanwhile, the addition of the phase noise introduces some inhomogeneity in the pulse-to-pulse phases. Despite this inhomogeneity in the phases, we still observe well isolated comb lines in the disordered Hatano-Nelson lattice. Specifically, we find that the largest secondary comb line is suppressed by 13.6 dB relative to the primary comb line.

Our results for the Hatano-Nelson lattice stand in stark contrast to our simulations for a trivial lattice with phase noise. In Fig. 21 we present a simulation of a trivial lattice with phase noise. While we expect the pulse-to-pulse amplitudes and phases to be uniform in the absence of disorder, in the presence of phase noise we find that both the pulse-to-pulse amplitudes and phases become inhomogeneous in the trivial lattice. The additional phase noise greatly degrades the quality of the frequency comb produced in this case, and the largest secondary comb line is only suppressed by 1.2 dB relative to the primary comb line.

The degradation of the frequency comb in the disordered trivial lattice relative to that in the disordered Hatano-Nelson lattice strongly suggests that the frequency comb produced by the topological Hatano-Nelson lattice is also robust against the addition of phase noise in the couplings.

8 Potential for Sensing Applications

In the main text, we observed that the temporally mode-locked state of our laser can be sensitive to the couplings. We showed this by introducing a boundary into the Hatano-Nelson couplings in our laser and observing that the temporally mode-locked state changed from being uniform to forming a nascent skin mode near the boundary of the lattice. In this section, we propose a model that can potentially exploit the sensitivity of our laser's temporally mode-locked state for sensing.

We show our proposed model in Fig. 22(a). Essentially, this model consists of N independent dimers. The coupling strengths in each dimer are asymmetric and, for all the dimers but one, the coupling strengths are w in one direction and $v < w$ in the other. The one remaining dimer, which we call the sensing dimer, has a coupling strength w in one direction and a coupling strength κ in the other direction. As we illustrate in Fig. 22(b), these dimers exhibit the Jordan block form of an exceptional point when $v = \kappa = 0$. However, instead of directly utilizing these exceptional points for sensing, we propose a sensor that relies on changing the coupling strength κ in the sensing dimer relative to the coupling strength v in the remaining dimers.

While the dimers in Fig. 22(a) are not directly coupled to one another, in our temporally mode-locked laser they still interact through the laser's nonlocal gain saturation. Therefore, changes in the coupling strength κ in the sensing dimer can influence the distribution of the laser's power between all the dimers in the system. When $\kappa < v$, the loss in the sensing dimer is greater than that in the other dimers, and we expect that lasing in the sensing dimer will be suppressed. In contrast, when $\kappa > v$, there is less loss in the sensing dimer than in the other dimers, and we expect that the sensing dimer will suppress lasing in the other dimers. We illustrate this in Fig. 22(c) by plotting the fraction of the lowest-loss eigenstate that is localized in the sensing dimer as a function of κ (here, $v/w = 0.5$). We see that there is a sharp transition from none of the state being in the sensing dimer to all the state being in the sensing dimer at $\kappa = v$.

Because Fig. 22(c) is calculated directly from the eigenstates, it does not include physics of our laser such as the Kerr nonlinearity. Therefore, we perform lumped element simulations of the model in Fig. 22(a) to better model the physics in our temporally mode-locked laser. For these simulations, we largely use the same parameters as in Sec. 5. However, to reduce the simulation time, we shorten the length of the dispersion shifted fiber to $L_{\mathrm{DSF}} = 0.5$ m, and we only consider 16 pulses (8 dimers). Moreover, we use $g_0 = 4.0$ m^{-1}, and we initialize our laser from a uniform background rather than simulating the effect of noise.
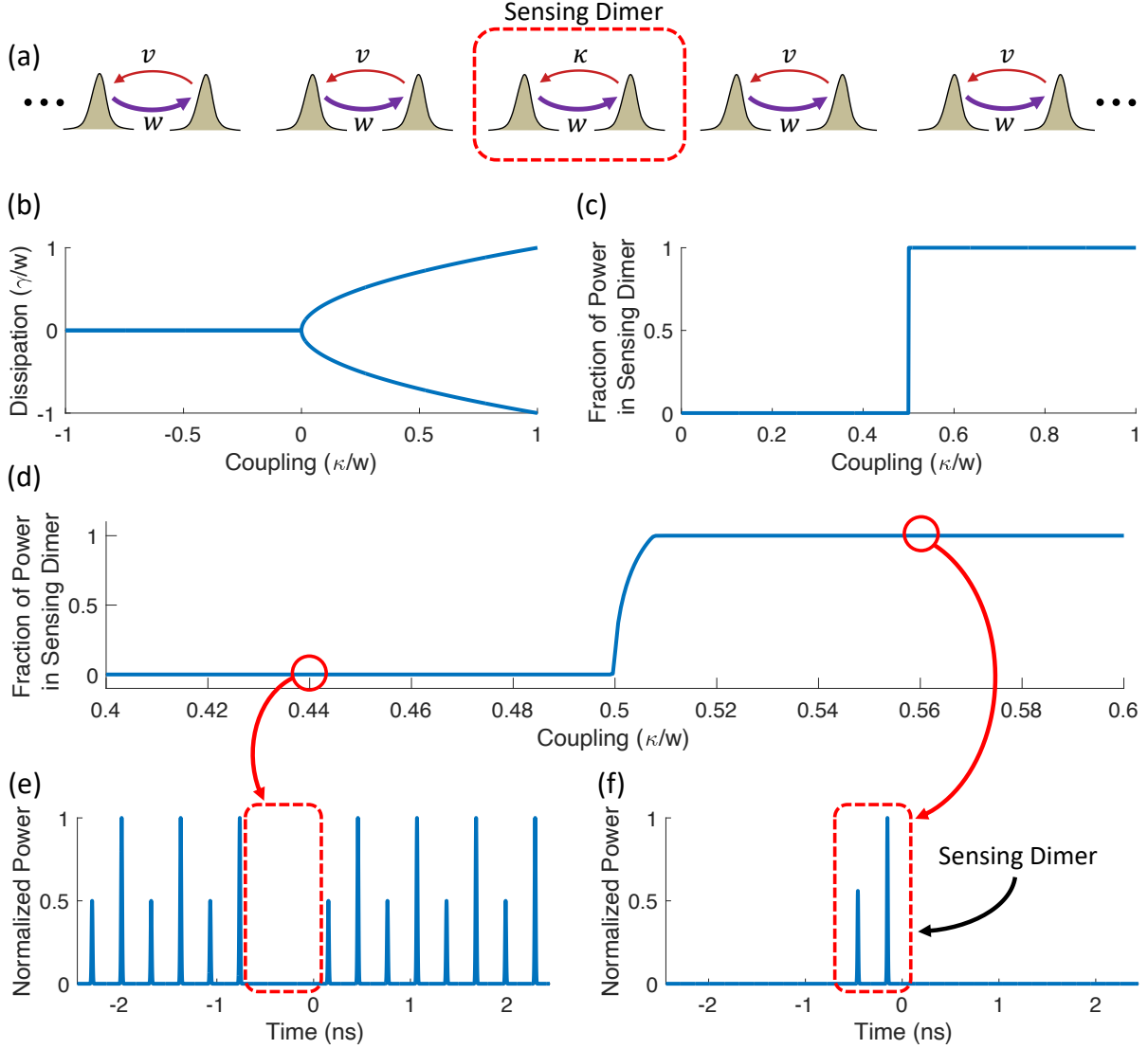
Figure 22: **Proposed Model for Sensing with a Temporally Mode-Locked Laser.** (a) Proposed model for sensing with a temporally mode-locked laser. (b) Eigenvalues of the sensing dimer, showing the presence of an exceptional point when $\kappa = 0$. (c) Expected fraction of the laser's power in the sensing dimer as a function of κ, determined from the eigenvalues of the linear lattice. (d) Simulated fraction of the laser's power in the sensing dimer as a function of κ with the Kerr nonlinearity included. In (c,d), $v/w = 0.5$. (e) Simulated state for $\kappa/w = 0.44$. (f) Simulated state for $\kappa/w = 0.56$.

In Fig. 22(d), we present the results of our simulations. We observe that the Kerr non-linearity "softens" the transition in the amount of power that localizes in the sensing dimer. Nonetheless, the amount of power localized in the sensing dimer still changes quite suddenly in the vicinity of $\kappa = v$. While additional considerations are necessary to determine whether this sudden change in the power localization can be used to construct a practical sensor, the rapid change observed in these simulations offers some evidence that such a sensor might be possible. Further exploring the possibility of sensing with temporally mode-locked lasers will be an interesting direction for future study.

9 Comparison with Earlier Work

In this section, we will compare our topological temporally mode-locked laser to earlier realizations of mode-locked lasers, topological lasers, and temporal synthetic dimensions. Our aim is to clarify how our topological temporally mode-locked laser differs from previous studies and to suggest possible advantages of using our topological temporally mode-locked laser for both practical applications and for studying non-Hermitian topological physics.

We begin by comparing our topological temporally mode-locked laser to "conventional" harmonically mode-locked lasers. Then, we compare our realization of temporal mode-locking to earlier realizations of temporal mode-locking. Third, we compare our topological temporally mode-locked laser with existing topological lasers. Finally, we discuss how our implementation of a temporal synthetic lattice differs from most other implementations of temporal synthetic lattices.

9.1 Comparison with Conventional Harmonically Mode-Locked Lasers

In the main text, we mentioned that a temporally mode-locked laser consists of three basic components, which are (I) a nonlocal nonlinearity, (II) a pulse formation mechanism, and (III) intracavity temporal couplings. We represent these three components schematically in Fig. 23.

In contrast to a temporally mode-locked laser, a conventional harmonically mode-locked laser only uses (I) a nonlocal nonlinearity and (II) a pulse formation mechanism. In a conventional harmonically mode-locked laser, the nonlocal nonlinearity might be slow gain saturation, while the pulse formation mechanism might be amplitude modulation at a harmonic of the cavity roundtrip frequency.

In the absence of any couplings, the phases of the pulses in the conventional harmonically mode-locked laser can evolve freely from one another, and this can preclude the use of these mode-locked lasers in frequency domain applications [10].

In stark contrast, our temporally mode-locked laser combines (I) a nonlocal nonlinearity and (II) a pulse formation mechanism with (III) intracavity couplings to lock the relative amplitudes and phases of the pulses in our mode-locked laser. As we discussed in Sec. 7 and Sec. 8, our ability to lock the relative amplitudes and phases can provide both practical advantages over
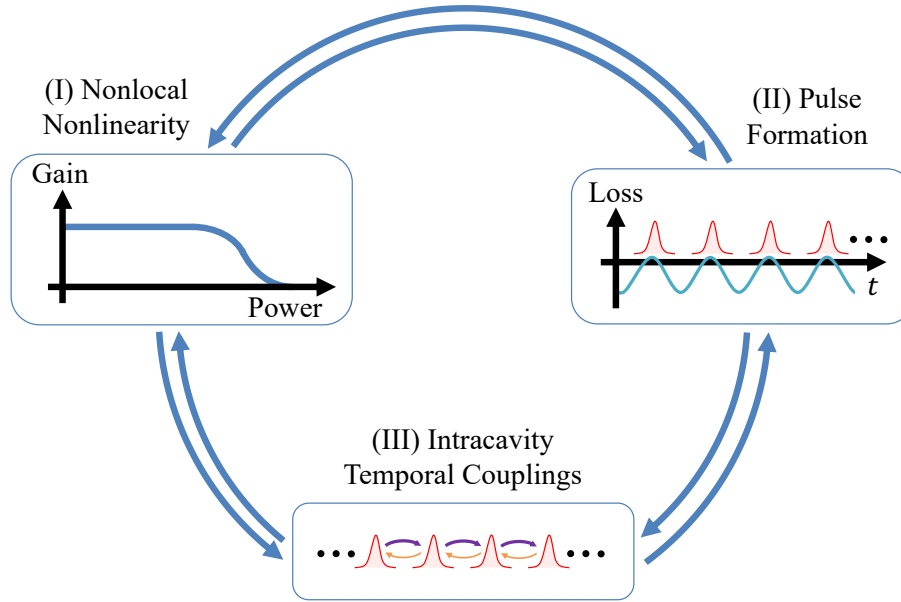
36

Figure 23: **Components of a Temporally Mode-Locked Laser.** Temporally mode-locked lasers consist of three basic components: (I) a nonlocal nonlinearity, (II) a pulse formation mechanism, and (III) intracavity temporal couplings. A conventional harmonically mode-locked laser only consists of components (I) and (II).

conventional harmonically mode-locked lasers and potentially enable novel applications that leverage the particular dynamics of temporal mode-locking.

9.2 Comparison with Other Temporally Mode-Locked Lasers

We use the term "temporal mode-locking" to describe the dynamics of our topological temporally mode-locked laser because we find that the dynamics of our laser are straightforwardly analyzed in terms of the laser's temporal modes. However, a simpler form of temporal mode-locking was previously investigated in mode-locked lasers as a method to suppress unwanted supermodes and to reduce supermode noise. Processes that force lasing in a single supermode are equivalent to temporal mode-locking because a single supermode describes a train of equally spaced, phase-locked pulses.

Two noteworthy architectures previously used intracavity couplings to study temporal mode-locking in harmonically mode-locked lasers. The first used a high-finesse, intracavity etalon to couple consecutive pulses in a mode-locked laser [10, 11]. In the frequency domain, this intracavity etalon filters out all but one of the supermodes in the mode-locked laser. A similar idea was achieved on an integrated platform using an intracavity ring resonator [12]. The second architecture used a composite cavity to suppress unwanted supermodes in a mode-locked laser. A preliminary study of the composite cavity approach found that, while this architecture
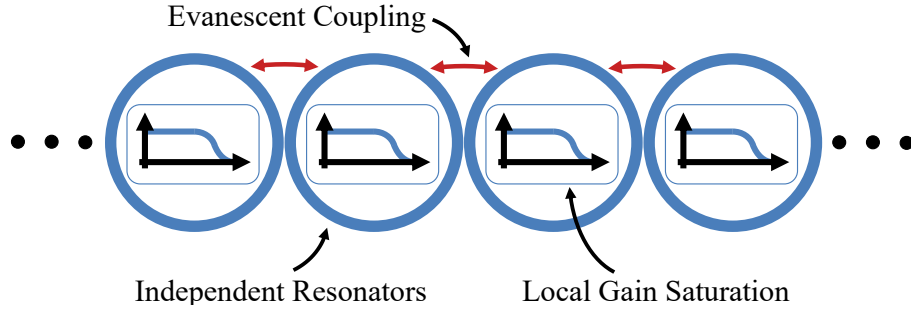
Figure 24: **Continuous-Wave Topological Lasers.** Many continuous-wave (CW) topological lasers consist of laser arrays composed of independent elements like the ring resonators shown here. Each ring resonator possesses its own gain medium, which saturates independently of the gain in the other resonators.

could suppress many of the supermodes in a mode-locked laser, it did not reduce the average supermode noise [13].

A major difference between our temporally mode-locked laser and previous mode-locked lasers with intracavity couplings is the level of complexity that we introduce into temporal mode-locking. Whereas previous efforts focused on isolating a single supermode of a mode-locked laser, we engineer the relative amplitudes and phases of the pulses in our mode-locked laser to realize nonuniform pulse patterns, such as the skin modes studied in the main text. Moreover, we show in simulation that topological temporal mode-locking can potentially give rise to robust topological frequency combs. To the best of our knowledge, these phenomena have not been previously explored.

9.3 Comparison with Continuous-Wave Topological Lasers

The use of a nonlocal nonlinearity in our topological mode-locked laser is a vital aspect of our work, and it stands in stark contrast to previous work on topological lasers.

Existing topological lasers [14, 15, 16, 17] have operated in the continuous-wave (CW) regime and have often relied on architectures like the one in Fig. 24. This architecture uses conservatively coupled spatial elements that each possess their own gain media. While these elements are represented by coupled ring resonators in Fig. 24, they could also be the components of a photonic crystal [18, 19, 20]. Together, the entire laser array forms a lattice.

Because each element in a CW topological laser contains its own gain medium, the gain saturates independently in each element of the laser array. As a result, experiments with CW topological lasers frequently pump only the edges of a topological laser or some other subset of the laser array to observe lasing in a topological edge state [15, 17, 19, 20].

In sharp contrast, in our mode-locked laser, all the sites (pulses) experience gain saturation due to the same gain medium, whose relaxation time is much slower than the cavity roundtrip period. In other words, our laser gain acts in a nonlocal way with respect to the topological
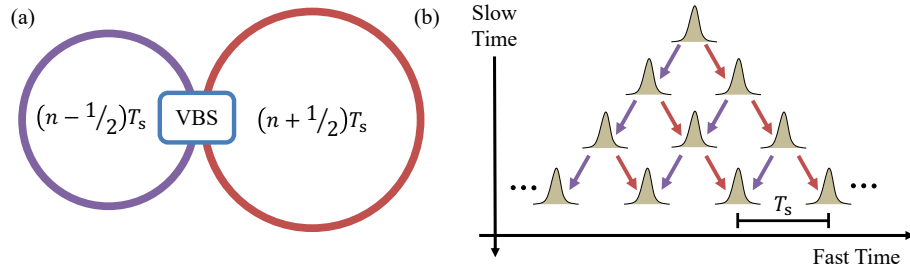
38

Figure 25: **Two-Loop Architecture for Photonic Mesh Lattices.** **(a)** The two-loop architecture consists of two fiber loops that are conservatively coupled with a variable beam splitter (VBS). **(b)** When a single pulse is excited in the two-loop architecture, it undergoes a random walk along the fast time axis (the time within a single roundtrip) as it propagates from roundtrip to roundtrip (along the slow time axis). This figure is based on that in [21].

lattice in our laser. This enables skin modes to spontaneously form in our mode-locked laser without us having to selectively pump the different sites in our synthetic temporal lattice.

9.4   Comparison with Two-Loop Architecture

In this subsection, we emphasize the architectural differences between the delay line couplings implemented in our topological temporally mode-locked laser and the "two-loop" architecture used to generate photonic mesh lattices in a temporal synthetic dimension. These differences have major implications for the types of physics that we can study in our temporally mode-locked laser.

In Fig. 25(a) we present a schematic of the two-loop architecture. This architecture consists of two fiber loops with staggered lengths that are conservatively coupled with a variable beam splitter. If the separation between two pulses in the mesh lattice is T_S, then the roundtrip delay through the larger loop is $(n + 1/2)T_S$, while the roundtrip delay through the shorter loop is $(n - 1/2)T_S$, for some integer n. As we show in Fig. 25(b), the staggered loop lengths create nearest-neighbor coupling between the sites of the mesh lattice. When a single site is excited, it undergoes a random walk, analogous to what occurs when a single waveguide is excited in a one-dimensional waveguide array.

Our delay line architecture, which we present in Fig. 26(a) stands in stark contrast to the two-loop architecture. The delay line architecture consists of a single resonant cavity (the "Main Cavity"), which supports N resonant pulses separted by T_R. On each roundtrip of the network, a portion of the light in the main cavity is siphoned off and passed through optical delay lines, which are designed to introduce couplings of certain lengths between the pulses in the network. In Fig. 26(b), we show how a delay line architecture with two delay lines can implement a one-dimensional synthetic lattice with nearest-neighbor couplings.

For over a decade, this two-loop architecture has enabled many groundbreaking photonic experiments, including photonic demonstrations of parity-time (PT) symmetric lattices [21, 22],
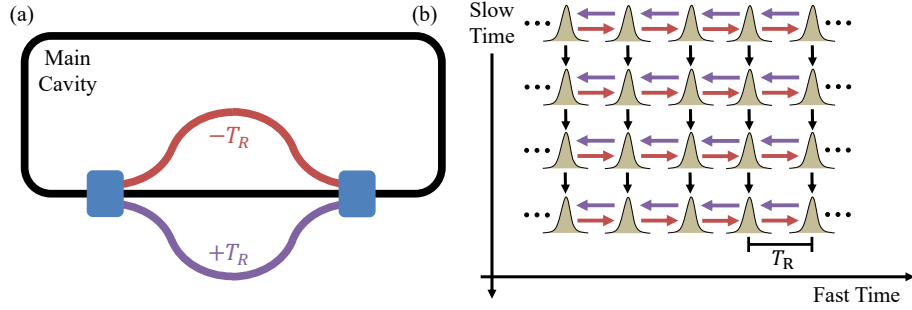
Figure 26: **Delay Line Architecture for Temporal Synthetic Dimensions.** **(a)** Our delay line architecture uses optical delay lines to implement dissipative couplings between the sites of a synthetic lattice. The main cavity supports N resonant pulses separated by a repetition period T_R. **(b)** On each roundtrip of the network (the slow time axis), the delay lines couple the sites of the synthetic temporal lattice, which is distributed along the fast time axis (the time within a single roundtrip). The black arrows represent the feedback from the main cavity, which propagates the states in the network from roundtrip to roundtrip.

topological funneling [1], and a topological triple phase transition [23]. However, there are several reasons why we use the delay line architecture for our topological temporally mode-locked laser rather than the two-loop architecture.

1. *The pulses in the two-loop architecture are not resonant within the individual loops.* In the two-loop architecture, the separation between the pulses in the loops is T_S, but neither loop has a length that is an integer multiple of the pulse-to-pulse separation. This makes the two-loop architecture unsuitable for harmonic mode-locking. In contrast, because the pulses in the delay line architecture are resonant, the main cavity in the delay line architecture may be converted into a harmonically mode-locked laser cavity.

2. *The couplings in the delay line architecture are inherently dissipative and nonreciprocal.* Dissipative couplings are an important feature of our topological temporally mode-locked laser because they enable us to engineer the gain and loss of the different states in our temporal synthetic lattices [2]. Nonlocal gain saturation then drives the laser's pulse pattern towards the lowest-loss state defined by the dissipative couplings. For this reason, the dissipative nature of the delay line couplings plays an important role in realizing the dynamics of topological temporal mode-locking.

   The couplings in our delay line architecture are also inherently nonreciprocal because one delay line controls only one direction of the coupling between two pulses. The nonreciprocal nature of the delay line couplings facilitates implementing non-Hermitian topological lattice models, such as the Hatano-Nelson model and the NH-SSH model, in our delay line architecture.

40

3. *The delay line architecture provides control over the boundary conditions.* Because the main cavity in the delay line architecture is a resonant loop, the "first" pulse sits next to the "last" pulse in our temporal synthetic lattices. This layout facilitates implementing periodic boundary conditions in the delay line architecture, and, by using intensity modulators in the delay lines, we can tune the boundary conditions of our temporal synthetic lattices. In our topological temporally mode-locked laser, this capability enables us to realize a nontrivial point-gap topological winding number in our synthetic Hatano-Nelson lattice and to study the Hatano-Nelson model under different boundary conditions.

   To the best of our knowledge, periodic boundary conditions have not been demonstrated with the two-loop architecture. Therefore, from this perspective, we believe that the delay line architecture may enable access to certain non-Hermitian topological physics that may not be possible to realize with the two-loop architecture.

4. *The delay line architecture is straightforwardly scalable to multiple synthetic dimensions and to lattices with long range couplings.* One major benefit of the delay line architecture studied in this work is its flexibility and scalability [2, 24]. By including delay lines of different lengths and by carefully engineering the mapping between the pulses in the main cavity and a particular synthetic lattice, the delay line architecture may be used to implement different lattice types, long-range couplings, and multiple synthetic dimensions.

References

[1] Weidemann, S. *et al.* Topological funneling of light. *Science* **368**, 311–314 (2020).

[2] Leefmans, C. *et al.* Topological dissipation in a time-multiplexed photonic resonator network. *Nat. Phys.* **18**, 442–449 (2022).

[3] Black, E. D. An introduction to Pound–Drever–Hall laser frequency stabilization. *Am. J. Phys.* **69**, 79–87 (2001).

[4] Haus, H. Mode-locking of lasers. *IEEE J. Sel. Top. Quantum Electron.* **6**, 1173–1185 (2000).

[5] Le Nguyen Binh & Ngo, N. Q. *Ultra-Fast Fiber Lasers: Principles and Applications with MATLAB® Models* (CRC Press, 2011), 1 edn.

[6] Zhang, K., Yang, Z. & Fang, C. Correspondence between Winding Numbers and Skin Modes in Non-Hermitian Systems. *Phys. Rev. Lett.* **125**, 126402 (2020).

[7] Gong, Z. *et al.* Topological Phases of Non-Hermitian Systems. *Phys. Rev. X* **8**, 031079 (2018).

[8] Hatano, N. & Nelson, D. R. Vortex pinning and non-Hermitian quantum mechanics. *Phys. Rev. B* **56**, 8651–8673 (1997).

[9] Hatano, N. & Nelson, D. R. Non-Hermitian delocalization and eigenfunctions. *Phys. Rev. B* **58**, 8384–8390 (1998).

[10] Quinlan, F., Ozharar, S., Gee, S. & Delfyett, P. J. Harmonically mode-locked semiconductor-based lasers as high repetition rate ultralow noise pulse train and optical frequency comb sources. *J. Opt. A: Pure Appl. Opt.* **11**, 103001 (2009).

[11] Harvey, G. T. & Mollenauer, L. F. Harmonically mode-locked fiber ring laser with an internal Fabry–Perot stabilizer for soliton transmission. *Opt. Lett.* **18**, 107–109 (1993).

[12] Srinivasan, S. *et al.* Harmonically Mode-Locked Hybrid Silicon Laser With Intra-Cavity Filter to Suppress Supermode Noise. *IEEE Journal of Selected Topics in Quantum Electronics* **20**, 8–15 (2014).

[13] Pottiez, O. *et al.* Supermode noise of harmonically mode-locked erbium fiber lasers with composite cavity. *IEEE Journal of Quantum Electronics* **38**, 252–259 (2002).

[14] St-Jean, P. *et al.* Lasing in topological edge states of a one-dimensional lattice. *Nature Photon* **11**, 651–656 (2017).

[15] Parto, M. *et al.* Edge-Mode Lasing in 1D Topological Active Arrays. *Phys. Rev. Lett.* **120**, 113901 (2018).

[16] Zhao, H. *et al.* Topological hybrid silicon microlasers. *Nat Commun* **9**, 981 (2018).

[17] Bandres, M. A. *et al.* Topological insulator laser: Experiments. *Science* **359**, eaar4005 (2018).

[18] Bahari, B. *et al.* Nonreciprocal lasing in topological cavities of arbitrary geometries. *Science* (2017).

[19] Zeng, Y. *et al.* Electrically pumped topological laser with valley edge modes. *Nature* **578**, 246–250 (2020).

[20] Dikopoltsev, A. *et al.* Topological insulator vertical-cavity laser array. *Science* **373**, 1514–1517 (2021).

[21] Regensburger, A. *et al.* Parity–time synthetic photonic lattices. *Nature* **488**, 167–171 (2012).

[22] Wimmer, M. *et al.* Observation of optical solitons in PT-symmetric lattices. *Nat Commun* **6**, 7782 (2015).

[23] Weidemann, S., Kremer, M., Longhi, S. & Szameit, A. Topological triple phase transition in non-Hermitian Floquet quasicrystals. *Nature* **601**, 354–359 (2022).

[24] Parto, M., Leefmans, C., Williams, J., Nori, F. & Marandi, A. Non-Abelian effects in dissipative photonic topological lattices. *Nat Commun* **14**, 1440 (2023).